Journal of Aerosol Science 160 (2022) 105899

Contents lists available at ScienceDirect

Journal of Aerosol Science

journal homepage: www.elsevier.com/locate/jaerosci

# Prediction of the carrier shape effect on particle transport, interaction and deposition in two dry powder inhalers and a mouth-to-G13 human respiratory system: A CFD-DEM study

Jianan Zhao [a], Ahmadreza Haghnegahdar [b], Yu Feng [a,*], Abhijeet Patil [c], Nandan Kulkarni [c], Gur Jai Pal Singh [c], Geena Malhotra [c], Rahul Bharadwaj [b]

[a] School of Chemical Engineering, Oklahoma State University, Stillwater, OK 74078, USA
[b] ESSS North America Inc., Woburn, MA 01801, USA
[c] Cipla R&D Center, Vikhroli (W), Mumbai 400083, India

ARTICLE INFO

*Keywords:*
Dry powder inhaler (DPI)
Computational fluid dynamics-discrete element method (CFD-DEM)
Spiriva™ Handihaler™ (SH)
Emitted aerodynamics particle size distribution (APSD)
Lung deposition
Comparability

ABSTRACT

Documentation of comparability between generic inhaler designs and the reference listed drug (RLD) inhalers is essential for regulatory approval of the products. Such assessments need high-fidelity numerical methods to accurately predict the transport, interactions, and deposition of orally inhaled drug products (OIDPs) in the human respiratory systems delivered *via* inhalers such as dry powder inhalers (DPIs). To explicitly model the particle-particle and particle-wall interactions for OIDPs, this study developed a computational fluid dynamics (CFD) and discrete element method (DEM) to examine drug delivery efficiency, determine emitted aerodynamic particle size distributions (APSDs), and quantify the resultant lung depositions of both lactose carriers and active pharmaceutical ingredient (API) particles. Numerical parametric studies were also performed with multiple actuation flow rates, carrier shapes, and DPI designs. Spiriva™ Handihaler™ (SH) and a generic DPI were selected in this study. The comparability assessment between the generic DPI and SH has been numerically performed. Specifically, CFD-DEM simulations were run at actuation flow rates of 30, 39, 60, and 90 L/min. Simulations were performed for both spherical and elongated lactose carrier particles with aspect ratios of 1, 5, and 10. Using the emitted APSDs as the mouth inlet conditions, the transport and deposition of API and lactose carriers from mouth to the tracheobronchial tree were also simulated. Numerical results indicate that with the same particle volume, the shape of lactose carriers can significantly influence the DPI delivery efficiency without a monotonic trend, due to the complex resuspension effect after deposition. However, the shape effect of lactose carriers is not significant on the lung deposition patterns of the API. Low actuation flow rates could potentially enhance the overall DPI-airway drug delivery efficiency. Using spherical lactose carriers, the comparability between the generic DPI and SH is demonstrated at all four actuation flow rates. The CFD-DEM model provides a feasible pathway on how to use CFD and DEM to evaluate the comparability between inhalers. The modeling framework also can help obtain new insights on transport dynamics of actines in DPIs to lung, thereby reducing the cost of generic product innovations and accelerating product review and approval.

* Corresponding author.420 Engineering North, Stillwater, OK, 74078, USA.
*E-mail address:* yu.feng@okstate.edu (Y. Feng).

https://doi.org/10.1016/j.jaerosci.2021.105899
Received 11 September 2021; Received in revised form 19 October 2021; Accepted 23 October 2021
Available online 3 November 2021

**Nomenclature**

*Acronyms*

| | |
|---|---|
| ANDA | Abbreviated new drug application |
| API | Active pharmaceutical ingredient |
| APSD | Aerodynamic particle size distribution |
| AR | Aspect Ratio |
| BE | Bioequivalence |
| CFD | Computational fluid dynamics |
| DEM | Discrete element method |
| COPD | Chronic obstructive pulmonary disease |
| DE | Delivery efficiency |
| DF | Deposition fraction |
| DPI | Dry powder inhaler |
| FDA | Food and drug administration |
| GDUFA | Generic drug user fee amendments |
| H-M | Hertz-Mindlin |
| JKR | Johnson-Kendall-Roberts |
| SH | Spiriva™ Handihaler™ |
| TI | Turbulence Intensity |
| OIDP | Orally inhaled drug product |
| PD | Pharmacodynamics |
| PK | Pharmacokinetics |
| RLD | Reference Listed Drug |
| ROA | Route of administration |

*Symbols*

| | |
|---|---|
| $a$ | Radius of contact |
| $A^{'}$ | Projected particle area in the flow direction |
| $C_D$ | Drag coefficient |
| $C_H$ | Normal damping coefficient |
| $d_p$ | Equivalent volume diameter for particles |
| $E^*$ | Effective Young's Modulus |
| $E$ | Young's Modulus |
| $\vec{F}_{BM}$ | Brownian motion induced force |
| $\vec{F}_c$ | Contact force |
| $\vec{F}_{cn}$ | Normal contact force |
| $\vec{F}_{cnadh}$ | Adhesion force predicted by the JKR cohesion model |
| $\vec{F}_{cnd}$ | Normal viscous damping force |
| $\vec{F}_{cne}$ | Normal elastic force |
| $\vec{F}_{ct}$ | Tangential contact force |
| $\vec{F}_{ctd}$ | Tangential viscous damping force |
| $\vec{F}_{cte}$ | Tangential spring force |
| $\vec{F}_{ctf}$ | Frictional force |
| $\vec{F}_D$ | Drag force |
| $\vec{F}_{fp}$ | Forces acting on particles by fluid flow |
| $\vec{F}_g$ | Gravitational force |
| $\vec{F}_L$ | Lift force |
| $\vec{F}_{pf}$ | Forces acting on fluid flow by particles |
| $\vec{F}_{VM}$ | Added (virtual) mass force |
| $\vec{F}_{\nabla p}$ | Pressure gradient force |
| $\vec{g}$ | Gravitational acceleration |

| | |
|---|---|
| $\vec{\vec{\imath}}$ | Unit tensor |
| $\vec{\vec{I}}$ | Moment of inertia tensor |
| $K_n$ | Normal contact stiffness |
| $\vec{M}_c$ | Torque generated by tangential forces |
| $\vec{M}_{fp}$ | Torque generated by flow velocity gradient |
| $m^*$ | Effective mass |
| $m_p$ | Mass of particle |
| $\vec{n}$ | Unit normal vector |
| $p$ | Pressure |
| $R^*$ | Effective radius |
| $s_n$ | Normal contact overlap |
| $\dot{s}_n$ | Time derivative of $s_n$ |
| $\vec{s}_\tau$ | Tangential relative displacement at the contact |
| $\dot{\vec{s}}_\tau$ | Tangential component of the relative velocity at the contact |
| $s_{\tau,max}$ | Threshold value of relative tangential displacement |
| $t$ | Physical time |
| $\vec{u}_f$ | Velocity of airflow |
| $\vec{u}_p$ | Velocity of particle |
| $V_c$ | Mesh cell volume |
| *Greek symbols* | |
| $\Gamma$ | Surface energy |
| $\varepsilon$ | Coefficient of restitution |
| $\eta$ | Damping ratio for the linear spring-dashpot model |
| $\eta_H$ | Normal damping ratio for the Hertzian model |
| $\eta_\tau$ | Tangential damping ratio |
| $\mu$ | Air viscosity |
| $\mu_d$ | Dynamic friction coefficient |
| $\mu_p$ | Friction coefficient |
| $\mu_s$ | Static friction coefficient |
| $\nu_f$ | Kinematic viscosity of air |
| $\rho_f$ | Density of air |
| $\rho_p$ | Density of particle |
| $\sigma$ | Poisson's ratio |
| $\bar{\bar{\tau}}_f$ | Local stress tensor |
| $\psi$ | Overall DPI-airway drug delivery efficiency |
| $\vec{\omega}_p$ | Angular velocity vector |

## 1. Introduction

Chronic lung diseases, such as asthma and chronic obstructive pulmonary disease (COPD), and their impact on human health is a globally growing concern (Lee et al., 2015). Treatment of these ailments includes a variety of interventions, with orally inhaled drug products (OIDPs) as the treatment of choice due to proven effectiveness in local delivery (Pramanik et al., 2021). Amongst the various choices of medical device delivering OIDPs, dry powder inhalers (DPIs) carry significance due to the absence of coordination aerosols and environmental concerns associated with the pressurized metered-dose inhalers (MDIs).

Spiriva™ Handihaler™ (SH) delivers an efficacious dose of active pharmaceutical ingredient (API) nanoparticles to designated lung sites, e.g., peripheral lung, to treat emphysema, one of the three contributors to COPD. Upon actuation via patient inhalation, a dry powder dosage under the influence of inspiratory airflow is entrained and deagglomerated by a variety of fluidization and dispersion mechanisms that are device-specific. In addition, dry powders also contain micron-sized carrier particles (e.g., lactose) to increase API particle dispersion, thereby improving the delivery efficiency (DE) of APIs to the peripheral lung.

In 2017, the US Food and Drug Administration (FDA) published the Generic Drug User Fee Amendments (GDUFA) to enable reviewers to assess abbreviated new drug applications (ANDAs) more efficiently with an emphasis on regulatory science enhancements of complex drug products, including OIDPs. For most orally administered drugs that reach their sites of action through systemic circulation, bioequivalence (BE) is demonstrated based on drug concentration in a relevant biologic fluid (e.g., plasma or blood). However, this approach is currently considered inadequate in the United States to establish BE (Sandell, 2021) of inhalation products

intended for local action, as the lung delivery does not rely on systemic circulation. Instead, the comparability between generic DPIs and the reference listed drug (RLD) DPIs is based on their (1) device delivery efficiency, (2) emitted aerodynamic particle size distributions (APSDs), (3) lung deposition, and (4) equivalent pharmacokinetics (PK) and Clinical/pharmacodynamics (PD) data, with the latter being an indicator of local delivery (Walenga, Babiskin, & Zhao, 2019).

Effective inhalation therapy using DPIs depends on the total mass of the API from the DPI mouthpieces and the APSDs (Lewis, Rouse, Singh, & Edge, 2017; Walenga et al., 2019). Thus, accurate predictions of emitted APSDs from DPIs and the resultant lung deposition of OIDPs is a first step to demonstrating the comparability between different designs of DPIs. However, achieving comparability in emitted APSDs and lung depositions is challenging since they are highly related to DPI performance, which is a function of interactions between the patient and device (i.e., breathing patterns) (Alzahrany & Banerjee, 2015; Kleinstreuer, Zhang, & Donohue, 2008), as well as drug particle characteristics. Specifically, a detailed understanding is needed for deagglomeration and agglomeration between APIs and carriers since they are the key mechanisms to influence the emitted APSD. Therefore, new insights into DPI product developments are critically needed, which requires support from high-resolution particle dynamics data provided by reliable numerical models in a cost-effective and time-saving manner. There is a need to develop an accurate computational model to provide high-resolution *in silico* supportive evidence on air-particle flow dynamics both in the DPI flow channel and in virtual human respiratory systems, which can predict particle transport and entrainment with particle-particle interactions, including agglomeration/deagglomeration explicitly.

The combination of Computational Fluid Dynamics (CFD) and Discrete Element Method (DEM) (Benque & Khinast, 2021; Mitani, Ohsaki, Nakamura, & Watano, 2020; Ponzini, Da Vià, Bnà, Cottini, & Benassi, 2021; Tong, Yang, & Yu, 2017; Tong, Zhong, Yu, Chan, & Yang, 2016; Yang, Wu, & Adams, 2015; Zheng, Leung, & Gupta, 2021) that can capture the individual interactions between particles and explicitly track the dry powder particle trajectories in the DPI and the human respiratory systems has been previously employed. Specifically, Tong, Yu, and Yang (2016) employed the CFD-DEM approach to investigate the underlying mechanisms of loose drug agglomeration using a T-shape pipe. Tong et al. (2017) also studied the aerosolization mechanism of carrier-based formulations using the CFD-DEM approach. However, both studies used simplified drug-device geometries, which did not consider the device design effect on the particle interaction mechanisms. Mitani et al. (2020) investigated the drug particle adhesion mechanism based on a combined CFD-DEM approach but only focused on the capsule chamber within the design of a DPI. Ponzini et al. (2021) discussed the possibility of validating a coupled CFD-DEM model to simulate NEXThaler® *via* a series of comparisons between simulation results and experimental data. However, the APSD data and its effect on API transport were not reported in that study. Benque and Khinast (2021) used a CFD-DEM approach to estimate the flow-induced effect on APSD dispersion in Aerolizer®. In this work, the number of particles simulated was reduced to 10,000, which is much lower than the real-world total particle count in millions (Chew & Chan, 2001), due to the insufficient computational resources. Additionally, the effect of APSD on the drug DE in the lung was not investigated. Although other research efforts have attempted to develop CFD-DEM models to predict agglomeration and deagglomeration of carriers and APIs in other DPIs (Yang et al., 2015), only a few CFD-DEM studies focused on SH and assessed the comparability between generic DPIs and SH, an RLD device (Meng, Chen, & Chen, 2019).

Meng et al. (2019) studied the effect of carrier size and surface morphology on the aerosolization of formulation in the SH using CFD-DEM modeling, while API and the overall drug DE in the lung were not investigated. There is still a lack of a numerical modeling framework that can predict the emitted APSDs from DPIs and the resultant lung deposition *via* oral inhalation. This is one of the

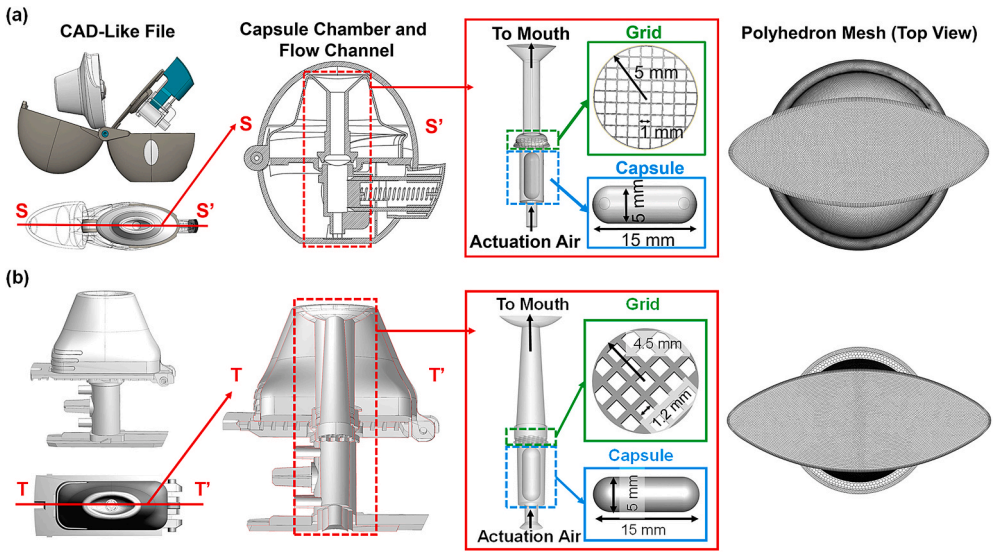


**Fig. 1.** Reconstructed DPI geometries and the hybrid polyhedral meshes including the flow channels, grids, and capsules for: (a) Spiriva™ Handihaler™ (partially reprinted from https://rocky.esss.co/blog/prediction-of-drug-particle-transport-in-a-dry-powder-inhaler-using-rocky-dem/) and (b) The generic DPI.

principal drivers for the present investigation. The other objective is the application of the CFD-DEM model to study the effect of particle shape on the drug powder DE to the human lung. This is important given that the particle shape engineering approach is a way to enhance the disaggregation of APIs and the DEM model has the advantage over other models, such as the discrete phase model (DPM), of capturing the particle shape effect and particle-particle interaction explicitly. Previous studies have demonstrated that elongated particles are more likely to reach lower airways (Feng & Kleinstreuer, 2013), indicating that controlling particle shape may be a way to increase small-airway depositions of orally inhaled medications. Also, with the progress in particle shape engineering for pulmonary drugs, customized shapes can be produced to meet medication customization demands (Chow, Tong, Chattopadhyay, & Shekunov, 2007; Zellnitz et al., 2019). Hence, it is of value to investigate how particle shape factors can be used to control particle aerodynamics and achieve targeted delivery to small airways.

Therefore, the objective of this study is to develop and test a computational tool based on CFD-DEM and computational fluid-particle dynamics (CFPD) to unveil the relationships between DPI design, lactose carrier shape, actuation flow rate between human and DPI, and the drug delivery efficiency to specific lung regions, i.e., after the 13th generation (G13). SH (Tiotropium Bromide as the RLD) and a generic DPI candidate were selected for the comparability assessment case study (see Fig. 1 (a) and (b)), as this comparison offered a typical design of single-dose and capsule-based devices, which can cover a broad range of flow resistance (Delvadia, Wei, Longest, Venitz, & Byron, 2016). The evaluation of the comparability between the generic DPI and SH has been numerically performed by comparing the DPI delivery efficiencies, emitted APSDs, and the resultant lung deposition patterns. The experimentally calibrated and validated CFD-DEM method was employed to predict agglomeration and deagglomeration of lactose carriers and APIs. CFD-DEM simulations were performed at steady actuation flow rates of 30, 39, 60, and 90 L/min (CDER, 2017). Other than particles in spherical shapes, simulations were also performed for sphero-cylindrical lactose carriers with an aspect ratio (AR) equal to 5 and 10. The resultant depositions of API and lactose carriers in a 3D human respiratory system (see Fig. 2) were predicted using the validated Euler-Lagrange based CFPD model (Feng & Kleinstreuer, 2013; Feng, Kleinstreuer, Castro, & Rostami, 2016; Feng, Kleinstreuer, & Rostami, 2015; Feng, Marchal, Sperry, & Yi, 2020; Feng, Zhao, Hayati, Sperry, & Yi, 2021; Haghnegahdar, Feng, Chen, & Lin, 2018; Haghnegahdar, Zhao, & Feng, 2019 a; Zhao, Feng, Bezerra, Wang, & Sperry, 2019). The API deposition after G13 is treated as an important contributor, assuming that the particles that escape from G13 outlets are considered deposited in the small airways with diameters less than 2 mm (Haghnegahdar, Zhao, Kozak, Williamson, & Feng, 2019 b; Zhao, Feng, Tian, Taylor, & Arden, 2021). Consequently, this study provides an enhanced understanding of the fundamental carrier-API interactions in DPIs, and the effect of lactose carrier shape and DPI flow channel designs on the drug delivery efficiency from DPI and the deposition patterns in a human respiratory system.

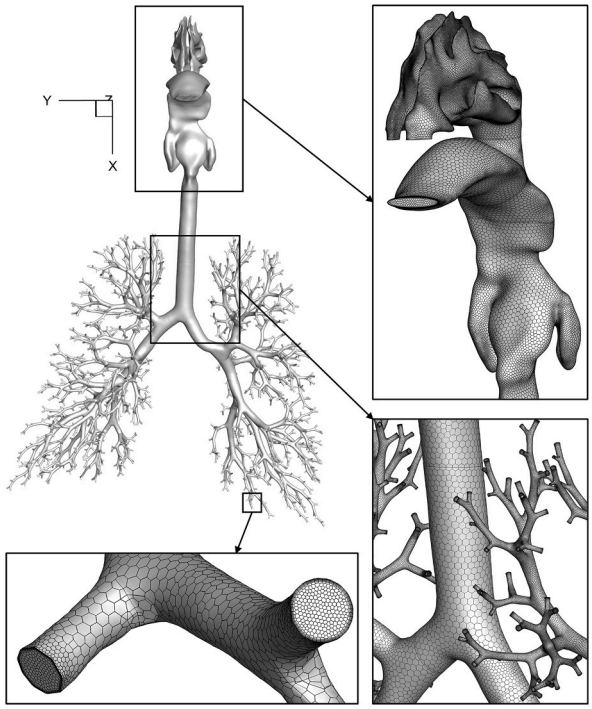


**Fig. 2.** Geometry and polyhedral mesh with near-wall prism layers of the human respiratory system.

## 2. Methodology

### 2.1. Geometry and mesh

The flow channels of SH and the generic DPI were constructed with capsules and grids included (see Fig. 1 (a) and (b)). The two flow channels contain:

(1) Elliptical actuation air inlets for SH and the generic DPI, respectively;
(2) Capsule chambers with a diameter of 7.5 mm and a length of 17.8 mm along the flow direction for SH, and similar dimensions for the generic DPI;
(3) Grids designed for separating the particle bulk flows (see Fig. 1 for geometry dimension details);
(4) Extended tubes with for SH and the generic DPI, respectively;
(5) Elliptic mouthpieces as the outlets connecting to the oral cavity with an area of 76 $mm^2$ for SH and a similar area for the generic DPI; and
(6) Capsules (5 mm in diameter and 15 mm in length) were positioned at the centers of the capsule chambers for both SH and the generic DPI.

The 3D human respiratory system geometry (see Fig. 2) was constructed by extending the mouth/nose-to-trachea geometry used in Zhang, Kleinstreuer, and Feng (2012) with a 3D tracheobronchial tree covering up to G13. A detailed description of the revised geometry and the corresponding mesh can be found in Hayati, Feng, and Hinsdale (2021). An overview of the airway geometry and CFD mesh is shown in Fig. 2.

Finite volume meshes were generated for the DPI flow channels using Ansys Fluent Meshing 2020 R2 (Ansys Inc., Canonsburg, PA). Meshes consist of polyhedral elements with near-wall prism layers to capture the laminar-to-turbulence transitions accurately using the Generalized k-ω (GEKO) turbulence model (Menter & Lechner, 2019). Based on the mesh independence test, the final meshes of SH and the generic DPI (see Fig. 1) have a total of 3,732,269 and 2,936,375 cells, respectively. The mesh independence tests were performed, and details can be found in Appendix A: Supplementary Data. A detailed description of the CFD mesh independence test and final mesh for the 3D human respiratory system employed can be found in a previous paper (Hayati et al., 2021). Specifically, 7,064,092 polyhedron-based cells were generated for the computational domain of the human respiratory system. To resolve the velocity gradient and precisely capture the laminar-to-turbulence transitions close to the wall, five near-wall prism layers were generated.

### 2.2. Governing equations

Accurate prediction of APSDs emitted from DPIs requires consideration of effects of particle-particle and particle-wall interactions (i.e., agglomeration and deagglomeration) during the drug particle transport simulations (Feng & Kleinstreuer, 2013, 2014). To address such complexity, a generalized one-way coupled CFD-DEM model (Feng & Kleinstreuer, 2013, 2014) with the Hertz-Mindlin (H-M) Johnson-Kendall-Roberts (JKR) cohesion model (Jiang, Dai, Cui, & Xi, 2018; Johnson, Kendall, Roberts, & Tabor, 1971) has been calibrated and validated. The validated CFD-DEM method can predict the particle agglomeration/deagglomeration and the resultant emitted APSDs in a computationally efficient manner. It is worth mentioning that the H-M JKR model can accurately describe the adhesion resulting from the short-range surface forces for studies of agglomeration at micro-/nano-scale, which is proved by many existing studies (Carrillo, Raphael, & Dobrynin, 2010; Horabik & Molenda, 2016; Jiang et al., 2018; Moreno-Atanasio, 2012; Wang et al., 2017).

For the air-particle flow dynamics simulations in the human respiratory system, the validated Euler-Lagrange based model, i.e., the computational fluid dynamics-discrete phase model (CFD-DPM) (Feng et al., 2018), was employed. Specifically, the turbulent airflow is simulated using the Reynolds averaged Navier-Stokes (RANS) approach considering its computational efficiency and accuracy compared with the large eddy simulation (LES) (Koullapis et al., 2018; Zhang & Kleinstreuer, 2011). For particle tracking, individual particle trajectories were calculated using the Lagrange method (Feng et al., 2018). Specifically, the particle trajectory and velocity were calculated by solving Newton's second law (Feng et al., 2018). Forces acting on the particles considered in this study are drag force, gravitational force, and Brownian motion induced force (Feng et al., 2018; Longest et al., 2019). The validation of the application of the customized CFD-DPM model in the oral/nasal cavities and TB tree has been well documented (Feng & Kleinstreuer, 2013; Feng et al., 2016; Feng et al., 2015; Feng et al., 2020; Feng et al., 2021; Haghnegahdar et al., 2018; Haghnegahdar et al., 2019 a; Zhao et al., 2019; Zhao, Feng, & Fromen, 2020).

#### 2.2.1. Continuous phase: air-particle mixture

In the CFD-DEM model employed in this study, airflow in DPI and human respiratory systems was treated as a continuous phase. In contrast, particles embedded in the airflow were treated as discrete phases and tracked using the Lagrange method with the particle-particle interactions modeled using DEM. Conservation laws of mass and momentum for the airflow can be given as

$$\nabla \cdot \vec{u}_f = 0 \tag{1}$$

$$\frac{\partial \vec{u}_f}{\partial t} + \left(\vec{u}_f \cdot \nabla\right)\vec{u}_f = -\frac{\nabla p}{\rho_f} + \frac{1}{\rho_f}\nabla \cdot \left(\bar{\bar{\tau}}_f\right) + \vec{g} \tag{2}$$

where $\bar{\bar{\tau}}_f$ is the local stress tensor, calculated by

$$\bar{\bar{\tau}}_f = \mu\left(\nabla \vec{u}_f + \nabla \vec{u}_f^{\,T}\right) \tag{3}$$

where $\mu$ is the molecular viscosity..

*2.2.2. Discrete phase: API and lactose carrier particles*

In this study, translations, rotations, and interactions of APIs and lactose carrier particles were both predicted. The force and torque balances for particle *j*, and the particle-particle interactions between particle *i* and particle *j* are shown in Fig. 3. Combining the Lagrange method and DEM based on our calibrated H-M model with the JKR cohesion model (Feng & Kleinstreuer, 2013, 2014; Johnson, 2016; Mindlin & Deresiewicz, 1953), the governing equations for the discrete phase (i.e., particle *j*) are given as

$$m_{p,j}\frac{d\vec{u}_{p,j}}{dt} = \sum_i \vec{F}_{c,ji} + \vec{F}_{fp,j} + \vec{F}_{g,j} \tag{4}$$

$$\bar{\bar{I}}_j \frac{d\vec{\omega}_{p,j}}{dt} = \begin{bmatrix} I_{xx} & I_{xy} & I_{xz} \\ I_{yx} & I_{yy} & I_{yz} \\ I_{zx} & I_{zy} & I_{zz} \end{bmatrix} \begin{bmatrix} \frac{d\omega_{p,j,x}}{dt} \\ \frac{d\omega_{p,j,y}}{dt} \\ \frac{d\omega_{p,j,z}}{dt} \end{bmatrix} = \sum_i \vec{M}_{c,ji} + \vec{M}_{fp,j} \tag{5 a and b}$$

where $m_{p,j}$ is the particle mass, $\vec{F}_{g,j}$ is the gravitational force, $\vec{F}_{c,ji}$ is the particle-particle or particle-wall contact force, $\vec{F}_{fp,j}$ is the total force acting on the particle *j* due to the fluid-particle interactions, $\bar{\bar{I}}_j$ is the moment of inertia 2nd-rank tensor, $\vec{\omega}_{p,j}$ is the angular velocity vector, $\vec{M}_{c,ji}$ is the contact torque induced by the tangential contact forces, and $\vec{M}_{fp,j}$ is the torque due to the airflow velocity

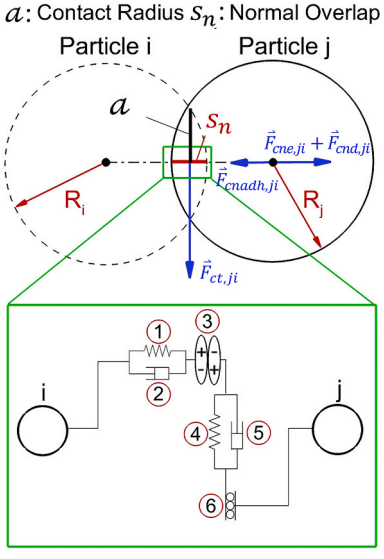


1: Normal Elastic Force - $\vec{F}_{cne,ji}$
2: Normal Viscous Damping - $\vec{F}_{cnd,ji}$
3: Adhesion Force - $\vec{F}_{cnadh,ji}$
4: Tangential Elastic Force - $\vec{F}_{ct,ji}$
5: Tangential Viscous Damping - $\vec{F}_{ctd,ji}$
6: Sliding Friction - $\vec{F}_{ctf,ji}$

**Fig. 3.** Particle force balance schematic with particle-particle interaction forces employed in the H-M model with JKR cohesion for DEM.

gradient.

$\vec{F}_{fp}$ in Eq. (4) accounts for the forces generated by the fluid on the particles, such as drag force $\vec{F}_D$, the pressure gradient force $\vec{F}_{\nabla p}$ (Shimazaki, Okubo, Yamamoto, & Yoshida, 2009), added (virtual) mass force $\vec{F}_{VM}$ (Johnson, 2016), lift force $\vec{F}_L$ (Saffman, 1965), the Brownian motion induced force $\vec{F}_{BM}$ (Li & Ahmadi, 1993), can be calculated using the Lagrange method by solving Newton's 2nd law for each particle, i.e.,

$$\vec{F}_{fp} = \vec{F}_D + \vec{F}_{\nabla p} + \vec{F}_{VM} + \vec{F}_L + \vec{F}_{BM} \tag{6}$$

The majority of these forces in Eq. (6) can be ignored. Specifically, since the density difference between fluid and particles is high ($\rho_p \gg \rho_f$), $\vec{F}_{VM}$ and $\vec{F}_L$ can be neglected. In addition, since the particle size is much smaller than the mesh cell size, $\vec{F}_{\nabla p}$ is negligible. Specifically, the typical mesh edge length is about 1 mm, whereas the median diameter of lactose and API are 46 μm and 2.8 μm, respectively. The details of drag coefficients ($C_D$) selections for both spherical and elongated sphero-cylindrical particles are presented in Appendix A: Supplementary Data.

To accurately model the deagglomeration and agglomeration behaviors among APIs and lactose carriers with different diameters from 1 to 200 μm (Calvert, Hassanpour, & Ghadiri, 2011; Kinnunen, Hebbink, Peters, Shur, & Price, 2014), the dominant adhesive forces, i.e., van der Waals force and electrostatic force, must be integrated into the DEM contact force model. Among the available adhesion DEM models, the H-M model with the JKR cohesion model (Johnson et al., 1971) has been assessed and validated for its capability to simulate the micro-/nano-scale powder packing process with the surface energy varying between 0.1 and 25 J/m$^2$ (Morrissey, 2013). The H-M model with the JKR cohesion model can describe the adhesion resulting from the short-range surface forces for studies of agglomeration at micro-/nano-scale (Carrillo et al., 2010; Horabik & Molenda, 2016; Jiang et al., 2018; Modenese, Utili, & Houlsby, 2012; Moreno-Atanasio, 2012; Walenga et al., 2019). Therefore, this study employed the H-M model with JKR cohesion to account for the adhesive behaviors between fine particles and introduced a cutoff value for the inter-particulate distance to avoid the numerical singularity at particle contact. Specifically, the adhesive contact force was modeled based on the balance between the stored elastic energy (i.e., normal and tangential elastic forces) and the loss in the surface energy (adhesion force). As stated above, it is assumed that the adhesion originated from van der Waals force and electrostatic force. The H-M model with JKR cohesion describes particle contacts as normally and tangentially damped harmonic oscillators with tangential friction $\vec{F}_{cn,ji}$ and an adhesion force $\vec{F}_{ct,ji}$. The JKR model includes the effect of elastic deformation, treats the effect of adhesion as surface energy only, and neglects adhesive stresses in the separation zone. Accordingly, inter-particle forces acting on particle $j$ from particle $i$ (see Fig. 3) can be modeled by the summation of two forces in normal and tangential directions, i.e.,

$$\vec{F}_{c,ji} = \vec{F}_{cn,ji} + \vec{F}_{ct,ji} \tag{7}$$

where $\vec{F}_{cn,ji}$ and $\vec{F}_{ct,ji}$ are normal and tangential contact forces, which can be expressed as

$$\vec{F}_{cn,ji} = \vec{F}_{cne,ji} + \vec{F}_{cnd,ji} + \vec{F}_{cnadh,ji} \tag{8}$$

$$\vec{F}_{ct,ji} = \vec{F}_{cte,ji} + \vec{F}_{ctd,ji} + \vec{F}_{ctf,ji} \tag{9}$$

In Eq. (8), $\vec{F}_{cne,ji}$ is the normal elastic force, $\vec{F}_{cnd,ji}$ is the normal viscous damping force, and $\vec{F}_{cnadh,ji}$ is the adhesion force in the JKR cohesion model (Johnson et al., 1971). Specifically, using the Hertz spring-dashpot model with JKR cohesion, the above-mentioned forces can be defined by

$$\vec{F}_{cne,ji} = \left(K_n s_n^{\frac{3}{2}}\right)\vec{n}_{ij} = \left(\frac{4}{3}E^*\sqrt{R^*}\, s_n^{\frac{3}{2}}\right)\vec{n}_{ij} \tag{10}$$

$$\vec{F}_{cnd,ji} = \left(C_H s_n^{\frac{1}{4}}\dot{s}_n\right)\vec{n}_{ij} = \left(2\eta_H\sqrt{m^* K_n}\, s_n^{\frac{1}{4}}\dot{s}_n\right)\vec{n}_{ij} \tag{11}$$

$$\vec{F}_{cnadh,ji} = \sqrt{8\pi\Gamma E^* a^3}\,\vec{n}_{ij} \tag{12}$$

where $K_n$ is the normal contact stiffness,$s_n$ is the normal contact overlap (see Fig. 2),$\dot{s}_n$ is the time derivative of $s_n$, $\vec{n}_{ji}$ is the unit normal vector, $a$ is the radius of contact between particles or between a particle and a boundary (see Fig. 2), $E^*$ is the effective Young's Modulus, $R^*$ is the effective radius, $C_H$ is the normal damping coefficient, $m^*$ is the effective mass, $\eta_H$ is the normal damping ratio for the Hertzian model, which can be defined as

$$\frac{1}{E^*} = \frac{1-\sigma_1^2}{E_1} + \frac{1-\sigma_2^2}{E_2} \tag{13}$$

$$\frac{1}{R^*}=\begin{cases}\dfrac{2}{d_{p,i}}+\dfrac{2}{d_{p,j}} & \text{particle}-\text{particle contact}\\ \dfrac{2}{d_p} & \text{particle}-\text{boundary contact}\end{cases} \tag{14}$$

$$\frac{1}{m^*}=\begin{cases}\dfrac{1}{m_{p1}}+\dfrac{1}{m_{p2}} & \text{particle}-\text{particle contact}\\ \dfrac{1}{m_p} & \text{particle}-\text{boundary contact}\end{cases} \tag{15}$$

$$\eta_H=\frac{\sqrt{5}}{2}\eta \tag{16}$$

In Eq. (13), $E_1$ and $E_2$ are Young's modulus of the two contacting particles or the particle and the boundary. In Eq. (14), $d_{p,i}$ and $d_{p,j}$ are the sizes of the contacting particles, and $d_p$ is the size of the particle in contact with the boundary. In Eq. (15), $m_{p1}$ and $m_{p2}$ are the mass of the contacting particles, and $m_p$ is the mass of the particle in contact with the boundary. In Eq. (16), $\eta$ is the damping ratio, a dimensionless parameter whose value is related to the restitution coefficient $\varepsilon$, which can be given by

$$\varepsilon=\begin{cases}exp\left[-\dfrac{\eta}{\sqrt{1-\eta^2}}\left(\pi-\tan^{-1}\dfrac{2\eta\sqrt{1-\eta^2}}{1-2\eta^2}\right)\right] & 0\le\eta<\dfrac{\sqrt{2}}{2}\\ exp\left(-\dfrac{\eta}{\sqrt{1-\eta^2}}\tan^{-1}\dfrac{2\eta\sqrt{1-\eta^2}}{2\eta^2-1}\right) & \dfrac{\sqrt{2}}{2}\le\eta<1\\ exp\left(-\dfrac{\eta}{\sqrt{\eta^2-1}}\ln\dfrac{\eta+\sqrt{\eta^2-1}}{\eta-\sqrt{\eta^2-1}}\right) & 1<\eta\end{cases} \tag{17}$$

where the restitution coefficient $\varepsilon$ is the user input that represents the particle-particle or particle-boundary interactions. It is also worth mentioning that the effect radius ($R^*$) can be calculated from the normal contact overlap $s_n$ by

$$s_n=\frac{a^2}{R^*}-\left(\frac{2\pi\Gamma a^2}{E^*}\right)^{\frac{1}{2}} \tag{18}$$

where $\Gamma$ is the surface energy.

Additionally, the tangential force $\vec{F}_{ct,ji}$ (see Eq. (7)) consists of the tangential spring force $\vec{F}_{cte,ji}$, the tangential viscous damping force $\vec{F}_{ctd,ji}$, and the frictional force $\vec{F}_{ctf,ji}$ (see Eq. (9)). $\vec{F}_{ct,ji}$ can be calculated using the Mindlin-Deresiewicz model (Mindlin & Deresiewicz, 1953), i.e.,

$$\vec{F}_{t,ji}=-\mu_p\left\|\vec{F}_{cn,ji}\right\|\left(1-\lambda^{\frac{3}{2}}\right)\frac{\vec{s}_\tau}{\left\|\vec{s}_\tau\right\|}+\eta_\tau\left(\frac{6\mu_p m^*\left\|\vec{F}_{cn,ji}\right\|}{s_{\tau,max}}\right)^{\frac{1}{2}}\lambda^{\frac{1}{4}}\dot{\vec{s}}_\tau \tag{19}$$

$$\lambda=\begin{cases}1-\dfrac{min\left(\left\|\vec{s}_\tau\right\|,s_{\tau,max}\right)}{s_{\tau,max}} & \left|\vec{s}_\tau\right|\le s_{\tau,max}\\ 0 & \left|\vec{s}_\tau\right|>s_{\tau,max}\end{cases} \tag{20}$$

where $\mu_p$ is the friction coefficient, $\eta_\tau$ is the tangential damping ratio estimated, $\vec{s}_\tau$ is the tangential relative displacement at the contact, $\dot{\vec{s}}_\tau$ is the tangential component of the relative velocity at the contact, and $s_{\tau,max}$ is the maximum relative tangential displacement at which particles begin to slide. Specifically, $\mu_p$ can be given as

$$\mu_p=\begin{cases}\mu_s & \text{no sliding at the contact}\\ \mu_d & \text{sliding at the contact}\end{cases} \tag{21}$$

in which $\mu_s$ and $\mu_d$ are the static and dynamic friction coefficients, respectively. The tangential damping ratio ($\eta_\tau$) can be given as

$$\eta_\tau=\frac{\ln\varepsilon}{\sqrt{\ln^2\varepsilon+\pi^2}} \tag{22}$$

**Table 1**
Particle material properties.

| Material Property | Tiotropium (Diulgheroff et al., 2012) | Lactose (monohydrate, α-) (Bassam, York, Rowe, & Roberts, 1990; DFE Pharma, 2006; Zuurman, Riepma, Bolhuis, Vromans, & Lerk, 1994) |
|---|---|---|
| Particle Density [kg/m$^3$] | 1530 | 1520 |
| Poisson's Ratio | 0.28 | 0.3 |
| Young's Modulus [MPa] | 46.7 | 1.68 |

*Note:* Young's moduli and Poisson's ratios were measured experimentally using Scanning Probe Microscopy (SPM).

The value of the maximum relative tangential displacement $s_{\tau,max}$ is determined by

$$s_{\tau,max} = \mu_p \left( \frac{1-\sigma_1}{2-\sigma_1} + \frac{1-\sigma_2}{2-\sigma_2} \right)^{-1} s_n \tag{23}$$

where $\sigma_1$ and $\sigma_2$ are the Poisson's ratios of the two particles or the particle and the boundary.

In addition, the eddy lifetime model is employed to account for particle interaction with turbulence eddies and the local turbulence fluctuation velocity components. It is worth mentioning that in the human respiratory system, particles were tracked using the Lagrange method by solving their individual trajectories using the validated CFPD method (Feng et al., 2016; Feng et al., 2015; Feng et al., 2020; Feng et al., 2021; Haghnegahdar et al., 2018; Haghnegahdar et al., 2019 a; Zhao et al., 2019). This study assumes that the drug particles escaped from G13 outlets are considered deposited/absorbed in the G13-to-alveoli region.

Moreover, the particle deposition in the human respiratory system is quantified using deposition fraction (DF), defined as the mass of deposited particles in a specific lung region divided by the total mass of particles entering the mouth (Tian, Hindle, Lee, & Longest, 2015).

### 2.3. Particle material properties

The API and excipient employed in this study are Tiotropium and lactose (monohydrate, α-), respectively. The material properties are summarized in Table 1. Specifically, the Poisson's Ratio and Young's Modulus of the API, as well as the cohesion/adhesion forces between API-API, lactose-lactose, and API-lactose, were measured using a commercial scanning probe microscopy (SPM) system (Asylum Research MFP-3D, Oxford Instruments Company) (Çalış, Öztürk Atar, Arslan, Eroğlu, & Çapan, 2019). The surface energies between APIs, carriers, and API-carrier are calibrated for the JKR model (Walton, 2008) (see Table 2 for the calibration results). The rest of the data were obtained from open literature (see Table 1).

### 2.4. Model verification, calibration, and validation

#### 2.4.1. CFPD model verification and validation

The details of the mesh independence test, CFD model verification, and CFD model validation are provided in Appendix A: Supplementary Data, which proves that the GEKO turbulence model (Menter & Lechner, 2019) can accurately predict the airflow fields in DPI flow channels, showing good agreements with the numerical simulation results using LES and the experimental measurements on pressure drops through the flow channels.

In addition, to build a reliable computational model that can accurately simulate the particle trajectories and airflow patterns in human respiratory systems, the particle phase model requires validation as well. The customized Lagrangian particle-tracking model has been validated *via* matching *in vitro* particle deposition fractions (DFs) in the oral/nasal cavities and TB tree, which is well documented in previous works (Feng & Kleinstreuer, 2013; Feng et al., 2016; Feng et al., 2015; Feng et al., 2020; Feng et al., 2021; Haghnegahdar et al., 2018; Haghnegahdar et al., 2019 a; Zhao et al., 2019).

#### 2.4.2. DEM model calibration

Calibration is required for the DEM model, since parameters such as surface energy between particles (both API and lactose) and DPI wall, static friction coefficient, as well as dynamic friction coefficient are important for the accurate predictions of the particle-particle interactions and emitted APSDs. Experimental measurements of the parameters mentioned above are challenging. As the alternative to direct measurements of those parameters, calibrations of friction coefficients and surface energy between particles and walls were performed using numerical simulations. Specifically, a range of surface energy values (from 0.01 to 10 J/m$^2$) have been tested in the CFD-DEM simulations to match the DPI delivery efficiency (i.e., fractions of drugs emitted from the DPI orifice) measured *in vitro*. Employing the actuation flow rate $Q_{in}$ = 39 L/min as a representative setup, CFD-DEM simulations were performed with different surface energies between particle and wall, the friction coefficient between particles, and friction coefficient between particle and wall (see Table 3 for the simulation results with different parameter values). The API delivery efficiency of SH DPI was compared with experimental data documented by FDA (FDA, 2004) for the parameter value calibrations. Determined by the best agreements on the delivery efficiencies between numerical results and experimental measurements (see Fig. 4), calibrated parameter values are listed in Table 2.

**Table 2**
Calibrated DEM properties for API and lactose particles.

| | API-API | API-Lactose | Lactose-Lactose | API-Wall | Lactose-Wall |
|---|---|---|---|---|---|
| Surface Energy Γ [J/m$^2$] | 43.4e-3 | 47.5e-3 | 13.4e-3 | 1.29 | 1.29 |
| Static Friction Coefficient | 0.7 | 0.7 | 0.7 | 0.5 | 0.5 |
| Dynamic Friction Coefficient | 0.7 | 0.7 | 0.7 | 0.5 | 0.5 |

**Table 3**
Particle (API + lactose) delivery efficiency of DPI by CFD-DEM simulations with different parameter values for calibration.

| ID | JKR Surface Energy Γ [J/m$^2$] | Friction Factor (Particle-Particle) [−] | Friction Factor (Particle-Boundary) [−] | Rolling Resistance [−] | API Delivery Efficiency [%] |
|---|---|---|---|---|---|
| 1 | 0.25 | 0.7 | 0.3 | non-rolling | 95.091 |
| 2 | 0.4 | 0.7 | 0.5 | non-rolling | 94.221 |
| 3 | 0.5 | 0.7 | 0.5 | non-rolling | 88.909 |
| 4 | 1 | 0.7 | 0.5 | non-rolling | 69.091 |
| 5 | 1.25 | 0.7 | 0.5 | non-rolling | 58.971 |
| 6 | 1.3 | 0.7 | 0.5 | non-rolling | 56.793 |
| 7 | 1.6 | 0.7 | 0.5 | non-rolling | 46.169 |
| 8 | 2 | 0.7 | 0.5 | non-rolling | 40.727 |
| 9 | 5 | 0.7 | 0.5 | non-rolling | 31.455 |

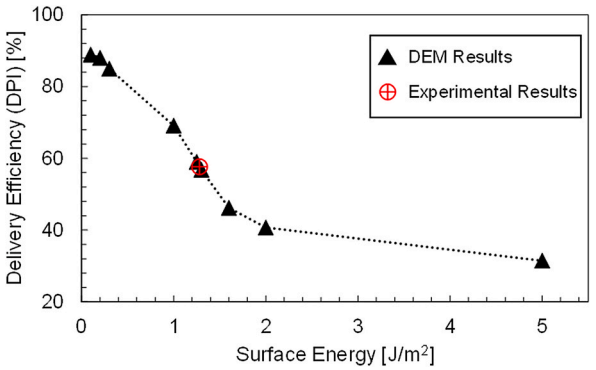


**Fig. 4.** The relationship between JKR particle-wall surface energy and the DPI delivery efficiency predicted by CFD-DEM simulations.

Specifically, to further determine the JKR surface energy between particles and the DPI wall, regressions were performed to correlate the relationship between the drug particle (mass) delivery efficiency and the JKR surface energy (see Fig. 4). It can be observed from Fig. 4 that the relationship between particle delivery efficiency is a linear function of particle-wall JKR surface energy when the surface energy is less than 2 J/m$^2$. The correlation can be given as

$$DE_{Lactose+API} = -43.56\Gamma_{particle-device} + 113.4 \qquad \Gamma_{particle-device} \in [0.4, 2]\mathrm{J/m^2} \tag{24}$$

Therefore, it can be determined that $\Gamma_{particle-device} = 1.29$ J/m$^2$. In addition, it can be further concluded that if the surface energy property between particles and DPI walls is reduced, the delivery efficiency is enhanced accordingly.

## 3. Numerical setup

Both CFD simulations of the airflow field in the DPI flow channel and CFPD simulations of pulmonary air-particle flow dynamics were performed using Ansys Fluent 2020 R2 (Ansys Inc., Canonsburg, PA) on a local Dell Precision T7810 workstation (Intel® Xeon® Processor E5-2643 v4 with dual processors, 64 cores and 128 GB RAM). The semi-implicit method for pressure-linked equations (SIMPLE) algorithm was employed for the pressure-velocity coupling, and the least-squares cell-based scheme was applied to calculate the cell gradients. The second-order scheme was employed for pressure discretization. In addition, the second-order upwind scheme was applied for the discretization of momentum and turbulent kinetic energy. Convergence is defined for continuity, momentum, and supplementary equations when residuals are less than 1.0e-5.

Coupled with CFD simulations of the airflow field in the DPI flow channel, DEM simulations were performed using Rocky 4.4.3 (ESSS, Woburn, MA) on local Dell Precision T7810 workstation (Intel® Xeon® Processor E5-2643 v4 with dual processors, 64 cores, and 128 GB RAM), Dell Precision 7920 Tower workstation (Intel® Xeon® Silver 4116 with dual processors and 128 GB RAM) with dual Quadro RTX 6000 GPUs, and the ESSS server (Intel® Xenon® CPU E5-2680 V3 @2.50 GHz (47 processors) with NVIDIA Titan V100

GPUs). The number of lactose and API particles released in the DPI capsule chambers are 7,166 and 1,713,008, respectively. The particle numbers are 1/10 of the real particle numbers in the SH DPI capsule. Indeed, using 1/10 of the API and lactose particles in CFD-DEM simulations can reduce 86% of the computational time and provide similar delivery efficiency (DE) predictions (i.e., less than 5% difference) compared with simulations using the realistic particle numbers in the capsule.

In-house user-defined functions (UDFs) were developed for (1) Measuring the emitted APSDs from the DPI orifices and converting them into particle release maps as the inlet conditions for lung aerosol dynamics simulations; (2) Specifying the transient inhalation profile at the mouth; (3) Recovering the anisotropic corrections on turbulence fluctuation velocities; (4) Modeling the Brownian motion induced force; and (5) Storing particle deposition data.

## 4. Results and discussion

### 4.1. Airflow structure in the SH flow channel

Distributions of normalized velocity magnitude ($\vec{V}/\overrightarrow{V_{in}}$) and turbulence intensity (TI) at four different actuation flow rates, i.e., $Q_{in}$ = 30, 39, 60, and 90 L/min, are shown in Fig. 5 (a) and (b). Specifically, the normalized velocity magnitude contours at plane z = 0 are shown in Fig. 5 (a). It can be observed that the maximum velocity locates at the bottom region of the capsule, due to the narrowed airflow passage with the presence of the capsule and the skewed velocity profiles near the capsule surface created by the airflow impingement. The velocity contours with $Q_{in}$ = 30 and 39 L/min share similar patterns in the computational domain near the capsule.

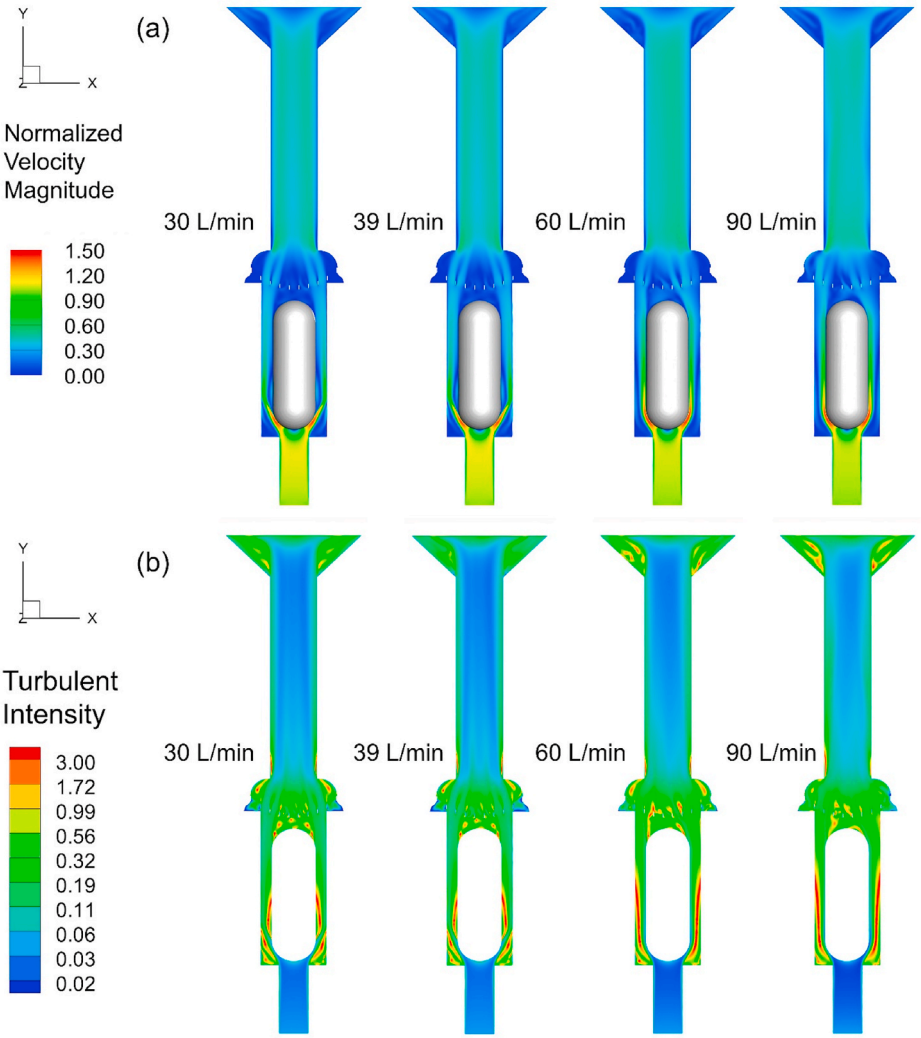


**Fig. 5.** Flow pattern at plane z = 0 in the SH DPI flow channel at different actuation flow rates (Qin = 30, 39, 60, and 90 L/min): (a) normalized velocity magnitude contours ($\vec{V}/\overrightarrow{V_{out}}$), and (b) turbulent intensity (TI) distributions.

Flow detachments can be found downstream the locations where the airflow impacts the capsule. At higher flow rates ($Q_{in}$ = 60 and 90 L/min), flow separations did not occur near the capsule bottom region. Instead, separation locations shift further downstream, compared with cases with $Q_{in}$ = 30 and 39 L/min. Indeed, with higher $Q_{in}$, the flow momentum after the impaction of the capsule remains higher. Therefore, the flow with higher $Q_{in}$ (i.e., 60 and 90 L/min) is able to conquer the viscous dissipation effect, and generate no flow separation near the capsule wall, compared with the flow with lower $Q_{in}$ (i.e., 30 and 39 L/min). Based on the TI comparisons shown in Fig. 5 (b), higher TI (i.e., TI > 3) can be observed near the wall of the capsule chamber in cases with higher $Q_{in}$ (i.e., 60 and 90 L/min). In contrast, for cases with $Q_{in}$ = 30 and 39 L/min, high TI (TI ≥ 300%) can be found only at the lower middle region near the capsule wall and the bottom region of the capsule chamber. TI is approximately 30% from the top of the capsule chamber to the mouthpiece. It can also be observed from Fig. 5 (b) that increasing $Q_{in}$ can elongate the high-TI cores as an indicator of stronger turbulence fluctuations.

### 4.2. *Particle deposition in the SH DPI flow channel and DPI delivery efficiency*

Localized particle deposition patterns in the SH DPI flow channel with different $Q_{in}$ and AR of lactose carrier particles are shown in Fig. 6. Here, AR is used to represent the aspect ratio of lactose only, since APIs investigated in this study are assumed to be quasi-spherical. At $Q_{in}$ = 30 and 39 L/min, the "hot spots" of lactose particle deposition are the surface of the capsule and the capsule chamber wall near the bottom opening of the chamber. Another concentrated deposition site for lactose particles is the grid region, especially for spherical lactose particles (AR = 1). At $Q_{in}$ = 60 or 90 L/min, the number of deposited lactose particles in DPI is less than in cases with $Q_{in}$ = 30 and 39 L/min. This is due to the more substantial resuspension effect induced by more intense aerodynamic forces (e.g., the drag force) acting on the deposited particles generated by higher airflow velocities. As a result, more deposited lactose and API particles are resuspended and transported along with the airflow downstream, and exited the mouthpiece. It can also be

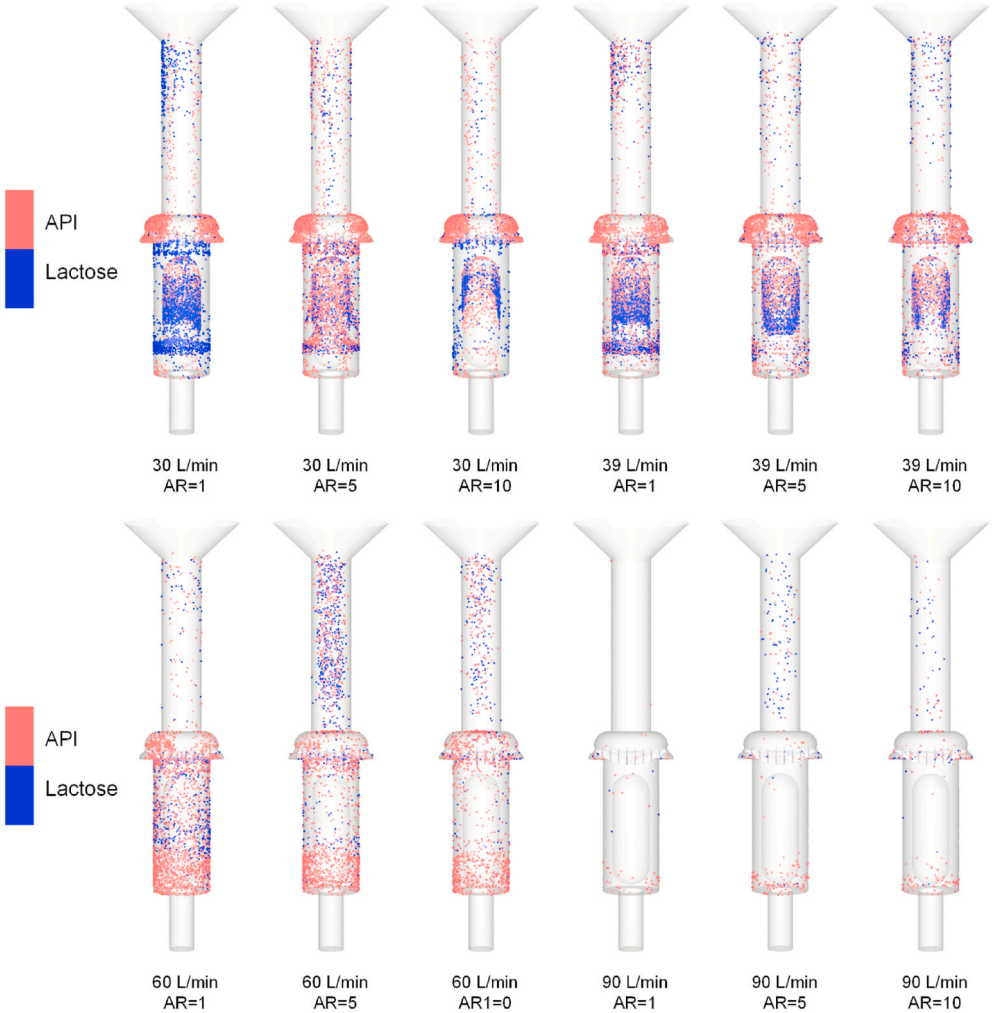


**Fig. 6.** Deposition distributions of API and lactose particles in SH DPI at different actuation flow rates ($Q_{in}$ = 30, 39, 60, and 90 L/min).

observed that the carrier particle shape has a noticeable influence on lactose deposition distributions in the DPI. Specifically, at $Q_{in}$ = 30 and 39 L/min, the deposited lactose in the capsule chamber decreases with the increasing lactose AR (also see Fig. 7 (b) for the total $DF_{lactose\text{-}DPI}$). Such an observation indicates that more elongated lactose carriers can deliver more particles into the mouth than the lactose carriers with more isotropic shapes and the same particle volume. At $Q_{in}$ = 60 L/min, with AR increase, fewer lactose particles are trapped in the capsule chamber but are deposited more downstream in the extending tube. Therefore, more elongated carrier particles can transport further downstream compared with more isotropic-shape particles with the same volume. This is mainly due to (1) the elongated particles are able to follow the airflow streams better than spherical particles with the same volume (Feng & Kleinstreuer, 2013); and (2) with the same particle volume, deposited elongated particles are easier to resuspend than particles in more isotropic shapes. Compared with cases at $Q_{in}$ = 60 L/min, similar deposition patterns can be observed in the cases with $Q_{in}$ = 90 L/min. However, at this flow rate, most of the lactose particles were emitted with the strongest convection effect generated by the highest $Q_{in}$, making the impact of AR on particle deposition distribution not evident for $Q_{in}$ = 90 L/min. Thus, Fig. 6 indicates that with the same particle volume, the more elongated lactose particles can be better at evading collision with the wall and more accessible to be resuspended by the airflow after deposition, which leads to less deposition in the DPI flow channel than expected from particles with more isotropic shapes.

For API particles, Fig. 6 shows that most API particles are deposited in the capsule chamber, capsule surface, and the cap wall above the grid for cases with $Q_{in}$ = 30 and 39 L/min. At $Q_{in}$ = 60 L/min, the number of APIs deposited on the cap wall and surface of the capsule is reduced compared with 30 and 39 L/min cases, while more API particles are deposited at the bottom of the capsule chamber. At $Q_{in}$ = 90 L/min, most API particles were emitted through the mouthpiece opening as there are few particles trapped either inside the capsule chamber or the cap wall.

The deposition fractions of API ($DF_{API\text{-}DPI}$) and lactose ($DF_{lactose\text{-}DPI}$) in the SH DPI flow channel are presented in Fig. 7 (a) and (b) with multiple $Q_{in}$ and AR. It can be observed from Fig. 7 (a) that the influence of lactose AR is not significant on $DF_{API\text{-}DPI}$ for cases with $Q_{in}$ = 60 L/min and 90 L/min since the turbulence dispersion effect is relatively more dominant. However, at $Q_{in}$ = 30 L/min, API deposition in the SH DPI reaches the maximum, i.e., $DF_{API\text{-}DPI}$ = 8.8%, with lactose AR = 5. This is possibly due to the combined effect of the variations in the easiness of deposition and resuspension with the lactose AR changes. Son, Longest, Tian, and Hindle (2013) investigated the dose delivery efficiency by SH DPI experimentally. Based on their results, the emitted dose mass fraction was 78.2% at $Q_{in}$ = 45 L/min, and the fine particle fraction of particles with $d_p \leq 5$ μm is 87.6% of the total emitted dose. There is approximately a

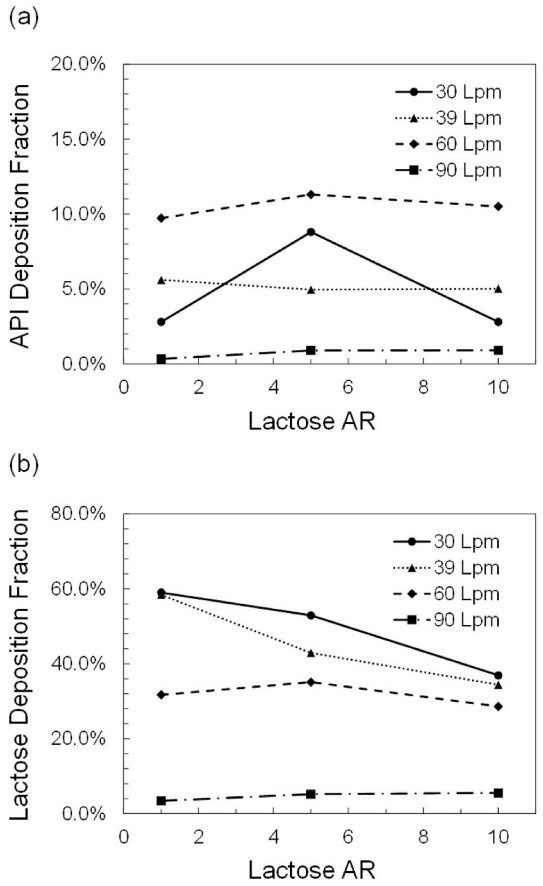


**Fig. 7.** Particle deposition fractions (DFs) *vs.* lactose AR in the SH DPI flow channel: (a) API, and (b) lactose.

10–15% difference in the $DF_{API\text{-}DPI}$ between the experimental results and our simulation results. The difference could be induced by two main reasons: (1) different $Q_{in}$, as Son et al. (2013) only presented the results at $Q_{in}$ = 45 L/min, and (2) different initial APSDs.

The impact of $Q_{in}$ on $DF_{API\text{-}DPI}$ is also shown in Fig. 7 (a), without a unified trend. Specifically, when AR = 1 or 10, the increase in $Q_{in}$ from 30 L/min to 60 L/min leads to the increase in $DF_{API\text{-}DPI}$. With the further increase in $Q_{in}$ from 60 L/min to 90 L/min, $DF_{API\text{-}DPI}$ decreases. Such non-monotonic trends are possibly due to the following mechanisms. Specifically, at lower $Q_{in}$, even though the convection effect is weaker than the high flow rate condition, the turbulent dispersion effect is also weaker (see Fig. 5 (a) and (b)). As a result, fewer APIs were deposited in the capsule chamber compared with 39 and 60 L/min cases. At high $Q_{in}$ (e.g., 60 L/min), the TI in the capsule chamber can reach as high as 300%, which leads to a high $DF_{API\text{-}DPI}$ in the bottom region of the capsule chamber (see Fig. 6 for the 60 L/min cases). Meanwhile, the deposited API in that region cannot be sufficiently resuspended by the aerodynamic forces, as the convection effect in the chamber at 60 L/min is not strong enough. As $Q_{in}$ increases to 90 L/min, the convection effect becomes more dominant and sufficiently strong to overcome the adhesion between API and the DPI wall. Therefore, APIs can resuspend more and be carried by the airflow to the DPI mouthpiece, which results in the decrease in $DF_{API\text{-}DPI}$ at $Q_{in}$ = 90 L/min compared with $Q_{in}$ = 60 L/min.

Lactose deposition fractions in the SH DPI ($DF_{lactose\text{-}DPI}$) influenced by both $Q_{in}$ and lactose AR are shown in Fig. 7 (b). $DF_{lactose\text{-}DPI}$ decreases significantly from 59% to approximately 6.0% as $Q_{in}$ increases from 30 to 90 L/min with spherical lactose carriers (AR = 1). Such trends imply that the turbulence has a weaker effect on the $DF_{lactose\text{-}DPI}$ than $DF_{API\text{-}DPI}$, since lactose carriers are much larger than APIs. Although the same trend between $DF_{lactose\text{-}DPI}$ and $Q_{in}$ is observed for elongated lactose carriers (AR = 10) with the same particle volume, $DF_{lactose\text{-}DPI}$ only decreases by 8.6% as the flow rate increases from 30 to 60 L/min. The decrease in $DF_{lactose\text{-}DPI}$ is less significant for the most elongated lactose carriers (AR = 10) because the flow exerts a smaller drag force on the elongated particles than the spherical particles with the same equivalent diameter, which means that the elongated particles are more likely to be emitted through the outlet. Specifically, when transported by the airflow, the major axis of the elongated particles is along the same direction of the airflow direction. Thus, the drag force acting on the elongated particles is reduced compared with spherical particles (Feng & Kleinstreuer, 2013).

For the lactose AR effect on $DF_{lactose\text{-}DPI}$ in the SH DPI, it can be found from Fig. 7 (b) that at $Q_{in}$ = 30 and 39 L/min, $DF_{lactose\text{-}DPI}$ decreases from approximately 50%–35%, with the increase in AR. The AR influence on DF is not evident when the flow rate reaches 60 and 90 L/min, as the total $DF_{lactose\text{-}DPI}$ fluctuates around 30% ($Q_{in}$ = 60 L/min) and 4% ($Q_{in}$ = 90 L/min), respectively. The non-monotonic relationship between $DF_{lactose\text{-}DPI}$ and lactose AR can also be due to combined influences from the variations in the easiness of deposition and resuspension with the lactose AR changes.

Based on Fig. 7 (a) and (b), it can be concluded that consideration of the particle resuspension, instead of using the idealized 100% trapped in the DPI wall, will enable the prediction of the more complex and realistic lactose shape effect on API and lactose transport and deposition. Overall, a high actuation flow rate ($Q_{in}$ = 90 L/min) and more elongated lactose carriers (AR = 10) can potentially

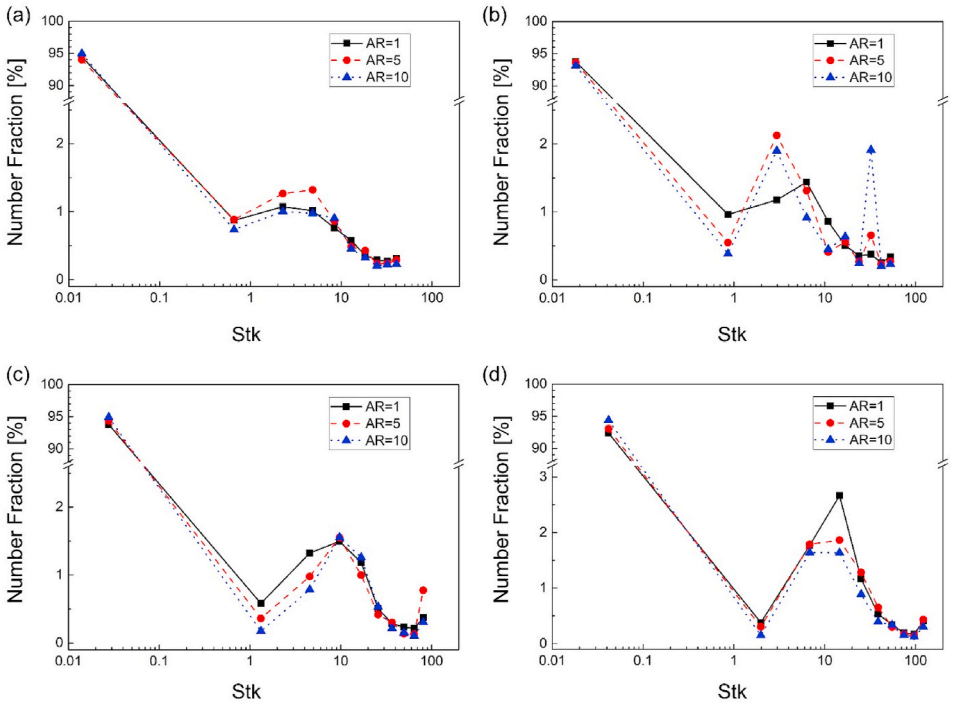


**Fig. 8.** Emitted APSDs from the SH DPI at different actuation flow rates: (a) $Q_{in}$ = 30 L/min, (b) $Q_{in}$ = 39 L/min, (c) $Q_{in}$ = 60 L/min, and (d) $Q_{in}$ = 90 L/min.

reduce the loss of API and lactose in SH DPI, thereby enhancing the delivery efficiency to the human mouth.

### 4.3. Effects of particle shape and actuation flow rate on the emitted APSDs using SH DPI

The effect of particle shape of lactose (AR) on emitted APSDs from the SH DPI is shown in Fig. 8 (a)-(d). The number fraction (NF) is defined as the number of particles within a specific size being divided by the total number of emitted particles, including both API and lactose. The Stokes number (Stk) is calculated based on the definition in (Hayati et al., 2021) of outlet airflow mean velocity of the DPIs. In general, when Stk is less than 1, the particles can follow the airflow path naturally. At $Q_{in}$ = 30 L/min, similar APSD patterns can be observed for Stk from 7 to 40 (particles with $d_p$ from 50 μm to 114 μm) for different lactose ARs (see Fig. 8 (a)). Moreover, the most elongated lactose (AR = 10) provided the highest NF (i.e., 95%) for small particles ($d_p \leq 4.3$ μm), which are mostly APIs. The case with $AR_{lactose}$ = 10 predicts lower NF for small particles due to the high NF of particles with $d_p$ = 90 μm predicted (see Fig. 8 (b)). At $Q_{in}$ = 60 and 90 L/min (see Fig. 8 (c) and (d)), use of more elongated carrier particles (AR = 10) predicted higher NF for small particles ($d_p \leq 4.3$ μm) than using carrier particles with less anisotropic shapes (AR = 1 and 5).

The effect of $Q_{in}$ on emitted APSDs is presented in Fig. 9 (a)-(c). $NF_{API}$ ($d_p \leq 4.3$ μm) are at a high level ranging from 92% to 96% for all $Q_{in}$ values. Indeed, using spherical lactose with AR = 1 (see Fig. 9 (a)), $NF_{API}$ decreases with the decrease in $Q_{in}$, since more lactose

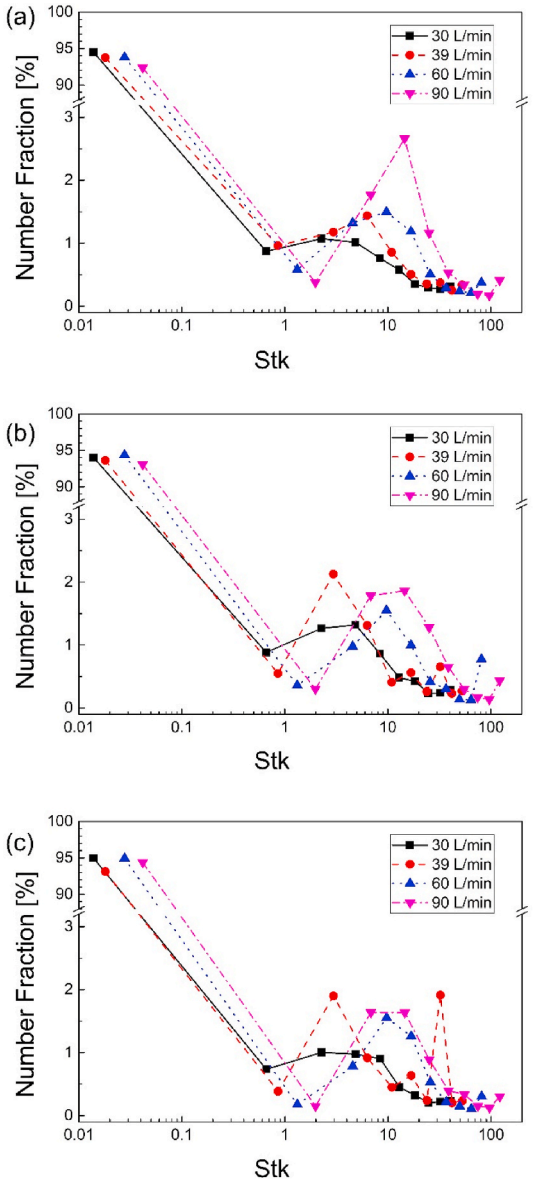


**Fig. 9.** Emitted APSDs from the SH DPI with different lactose AR: (a) AR = 1, (b) AR = 5, and (c) AR = 10.

particles with large size ($d_p$>30 μm) were emitted at a higher flow rate (also see Fig. 6). For particles (10 μm<$d_p$<60 μm), $NF_{lactose}$ increases with the increase in $Q_{in}$, which is consistent with the observations in Figs. 6–8). Especially for $Q_{in}$ = 90 L/min, the NF of particles with $d_p$ = 40 μm reaches 2.7%. With elongated lactose (AR = 5) shown in Fig. 9 (b), cases with all $Q_{in}$ values predict a similar trend of APSDs as the cases using spherical lactose (AR = 1) (see Fig. 9 (a)). Specifically, $Q_{in}$ = 90 L/min case predicts the lowest $NF_{API}$ (i.e., 93.1%) for all $Q_{in}$ values. For particles with $d_p$>20 μm, high $Q_{in}$ cases (i.e., 60 and 90 L/min) generate higher $NF_{lactose}$ than the case with low flow rate (i.e., $Q_{in}$ = 30 L/min). In contrast, when AR = 10 (see Fig. 9 (c)), $Q_{in}$ = 39 L/min leads to the lowest $NF_{API}$ ($d_p$≤4.3 μm) compared with $Q_{in}$ = 30, 60, and 90 L/min cases. For all four $Q_{in}$ setups, $NF_{lactose}$ ($d_p$>20 μm), high $Q_{in}$ cases (i.e., 39, 60, and 90 L/min) tend to generate higher $NF_{lactose}$ than the case with low flow rate (i.e., $Q_{in}$ = 30 L/min).

### 4.4. Airflow structure in the human respiratory system using the SH DPI

The inspiratory airflow structures at the sagittal plane y = 0 for the 3D human respiratory system employed in this study (see Fig. 2) are shown in Fig. 10 (a) and (b). It should be noted that the human mouth entrance has the same elliptic shape as the mouthpiece of the SH DPI. The highest flow velocity occurs at the mouth entrance due to the narrowed mouth opening area (see Fig. 10 (a)). When the inhalation flow rate, which is equal to the actuation flow rate $Q_{in}$, increases to 90 L/min, the airflow recirculation in the oral cavity is more noticeable near the upper palate, and the laryngeal jet becomes stronger. The turbulent kinetic energy (TKE) visualized in Fig. 10 (b) also demonstrates an increasing turbulence fluctuation in the oral cavity and oropharynx with the increase in $Q_{in}$.

### 4.5. Effects of $Q_{in}$ and AR on particle deposition in the human respiratory system using SH DPI

To investigate how $Q_{in}$ and lactose AR can influence lung depositions of lactose carriers and API particles, localized deposition distributions of lactose (AR = 1) and its regional deposition fractions (RDFs) in the airway model at different actuation flow rates ($Q_{in}$ = 30, 39, 60, and 90 L/min) with AR = 1, 5, and 10 are shown in Fig. 11 (a) and (b), respectively. Furthermore, Fig. 12 (a) and (b) show the lung deposition patterns of API and $RDF_{API\text{-}lung}$ with different $Q_{in}$ and lactose ARs, respectively. It is worth mentioning that this section focuses on the resultant airway deposition using the SH DPI. The emitted APSDs from the SH DPI with specific $Q_{in}$ and lactose AR (see Figs. 8 and 9) were applied as the mouth inlet conditions for the particle tracking in the human respiratory systems. Comparisons of SH and generic DPI induced lung deposition are discussed in Sections 4.8 and 4.9.

Based on the lung deposition data predicted using the CFPD model, all the lactose carrier particles are trapped in the oral cavity,

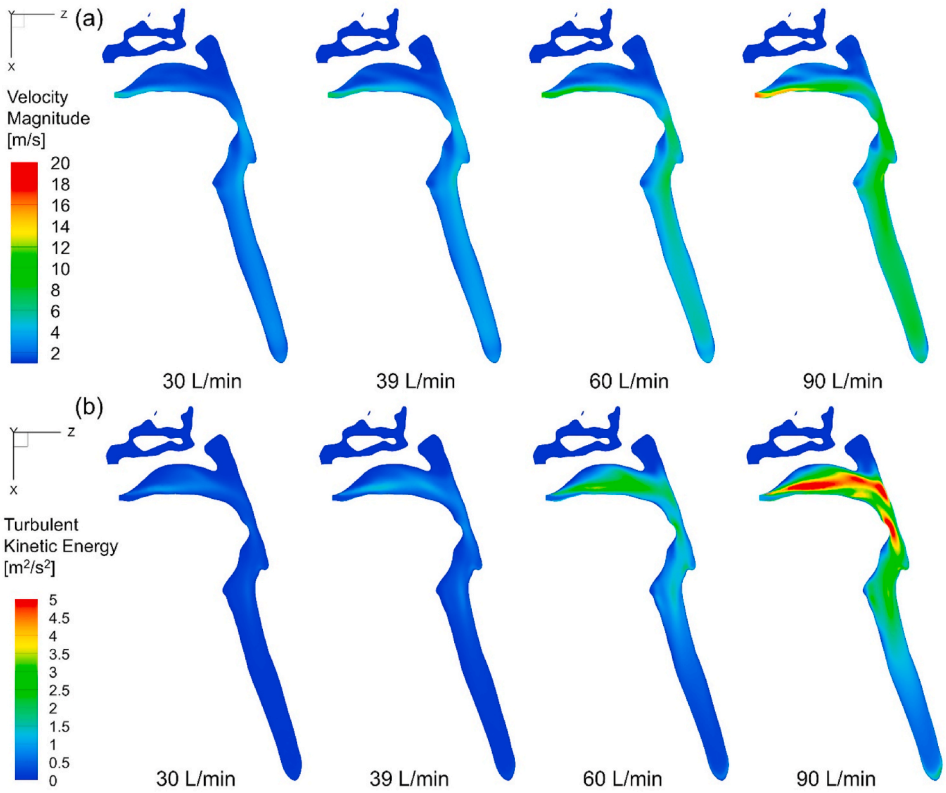


**Fig. 10.** Airflow characteristics at the sagittal plane y = 0 in the human respiratory system with different actuation flow rates ($Q_{in}$ = 30, 39, 60, and 90 L/min): (a) velocity magnitude contours and (b) turbulent kinetic energy contours.

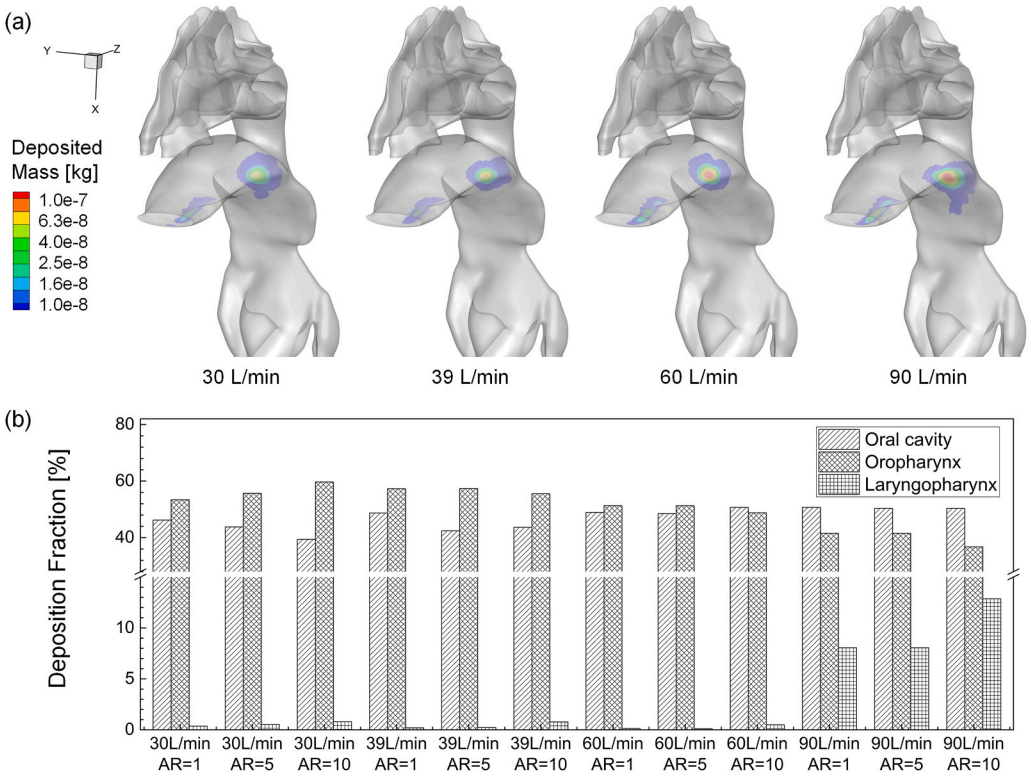


**Fig. 11.** Lactose deposition patterns in the upper airway at different actuation flow rates ($Q_{in}$ = 30, 39, 60, and 90 L/min) using SH DPI: (a) deposition distributions with lactose AR = 1 and (b) regional deposition fractions (RDFs) with lactose AR = 1, 5, and 10.

oropharynx, and laryngopharynx (see Fig. 11 (a)), despite $Q_{in}$ and AR variations. The lactose deposited on the tongue is mainly due to the inertial impaction of the mouth jets shown in Fig. 10 (a) and particle gravitational sedimentation, which are the two dominant deposition mechanisms for lactose particles with $d_p$>50 μm. Other deposition locations for lactose are at the posterior of the oropharynx and laryngopharynx. This is due to the impaction of the mouth jet after striking the tongue (see Fig. 10 (a)). For the regional deposition fraction of lactose ($RDF_{lactose\text{-}lung}$), several observations can be made based on the results shown in Fig. 11 (b), i.e., (1) At $Q_{in}$ = 30 and 39 L/min, the $DF_{lactose\text{-}oral\ cavity}$ decreases with the increase in AR, while at $Q_{in}$ = 60 and 90 L/min, AR has negligible influence on $DF_{lactose\text{-}oral\ cavity}$; (2) At low $Q_{in}$ = 30 L/min, the $DF_{lactose\text{-}oropharynx}$ increases with the increase in AR, while at $Q_{in}$ = 39, 60 and 90 L/min, $DF_{lactose\text{-}oropharynx}$ decreases with AR; and (3) $DF_{lactose\text{-}laryngopharynx}$ increases with the increase in AR for all $Q_{in}$. These observations demonstrate that for lactose carriers with the same volume, relatively elongated lactose (AR = 10) can follow the mainstream of the airflow better than spherical lactose (AR = 1) and deposit more downstream in the human upper airway. However, due to the large size ($d_p$>50 μm) of the lactose carriers, they were not able to reach the trachea and beyond.

For API deposition comparisons in human respiratory systems, Fig. 12 (a) and (b) show that with the increase in $Q_{in}$, more API particles are deposited in the oropharynx, glottis, trachea, and G1-G13 due to the enhanced inertia impaction effects. For example, with spherical lactose (AR = 1), when the $Q_{in}$ increases from 30 to 90 L/min, the DF of API in the upper airway (from mouth to G2) increases from 26.6% to 57.3% (see Fig. 12 (b)). Moreover, the stronger laryngeal jet effect at 90 L/min also results in the highest DF of API in the G0-G1 region (8.8%) compared with 4.1% at 30 L/min, 5.0% at 39 L/min, and 6.0% at 60 L/min (see Fig. 12 (b)). A high actuation flow rate not only leads to high DF of API in the upper airway (Mouth to G2), which is not optimal in terms of drug delivery efficiency, but also reduces the DF of API in the lower airway (after G13) and lowers the API delivery efficiency. For example, with spherical lactose carriers (AR = 1), the $DF_{API}$ in G13-to-alveoli region decreases by 38.2% (i.e., more than half) when $Q_{in}$ increases from 30 to 90 L/min. In terms of the effect of AR on the DF of API in the airway, Fig. 12 (b) shows that at the same $Q_{in}$, lactose AR has little effect on the API regional deposition fractions in all three regions. To quantify the delivery efficiency to the designated lung sites for deeper-airway COPD and/or asthma treatment, overall DPI-airway drug delivery efficiency $\psi$ is defined (see Table 4 for the definition of $\psi$) and calculated. The $\psi$values with different $Q_{in}$ and lactose ARs are listed in Table 4. The result demonstrates that low $Q_{in}$ (i.e., 30 L/min) is favored to achieve the higher overall drug delivery efficiency using the SH DPI, and $Q_{in}$ is the dominant factor on the regional API DF after G13 compared with the particle shape of lactose carriers.

### *4.6. Airflow structure in the generic DPI flow channel*

To assess the comparability of the generic DPI (see Fig. 1 (b)) in terms of drug delivery efficiency compared with the SH DPI, CFD-

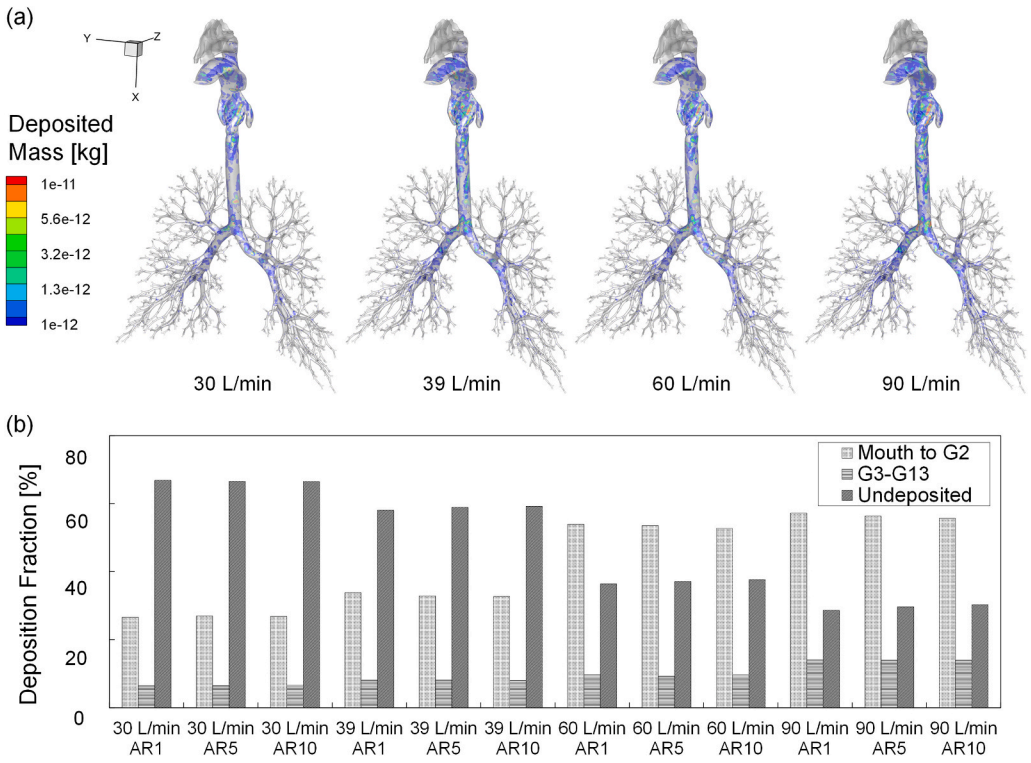


**Fig. 12.** API deposition patterns in the human respiratory system at different actuation flow rates ($Q_{in}$ = 30, 39, 60, and 90 L/min) using SH DPI: (a) deposition distributions with AR = 1 and (b) regional deposition fractions (RDFs) with AR = 1, 5, and 10.

**Table 4**
The overall DPI-airway drug delivery efficiencies ($\psi$)[a] *vs.* AR and $Q_{in}$.

| SH DPI | | | | |
|---|---|---|---|---|
| AR | 30 L/min | 39 L/min | 60 L/min | 90 L/min |
| 1 | 65.0% | 54.8% | 32.9% | 28.6% |
| 5 | 60.7% | 56.0% | 32.9% | 29.4% |
| 10 | 64.7% | 56.3% | 33.7% | 30.0% |
| Generic DPI | | | | |
| AR | 30 L/min | 39 L/min | 60 L/min | 90 L/min |
| 1 | 59.3% | 55.2% | 34.1% | 28.0% |

[a] $\psi = \dfrac{\textit{Deposited API after G13}}{\textit{Total amount of API injected into the DPI}} \times 100\% = (1 - DF_{API-DPI})DF_{API-after\ G13}$

DEM simulations were performed using a generic DPI model. Since it has been demonstrated that the lactose AR has a minimal influence on the API DF in both the SH DPI and the respiratory systems (see Sections 4.2 and 4.5), only lactose carriers with AR = 1 were employed for generic DPI simulations.

To evaluate the comparability of airflow fields between SH and generic DPI, airflow characteristics in the generic DPI channel with different $Q_{in}$ are shown in Fig. 13 (a) and (b). In contrast to the variations of flow separation locations with $Q_{in}$ in the SH DPI flow channel (see Fig. 5 (a)), the normalized velocity magnitude contours in the generic DPI flow channel shown in Fig. 13 (a) are similar and less influenced by $Q_{in}$. Specifically, no flow separation exists near the bottom of the capsule. In addition, the capsule chamber is a straight pipe with a constant diameter for SH, while the diameter of the chamber of generic DPI increases gradually in the mainstream direction. Hence, the reverse pressure gradient is less in the generic DPI capsule chamber than in the SH, which is sufficiently low and avoids the generation of flow separation at all $Q_{in}$. As shown in Fig. 13 (b), the difference in TI distribution is less noticeable among the four cases with different $Q_{in}$ in the generic DPI than in the SH (see Fig. 5 (b)). Furthermore, it can be observed that the TI near the capsule bottom region increases with the increase in $Q_{in}$, indicated by the more extended high-TI cores with the potentially higher turbulence dispersion with the higher Reynolds number. The differences in airflow patterns and geometric designs between the two DPI flow channels can potentially influence the comparability of particle transport, interaction, and deposition, discussed in the

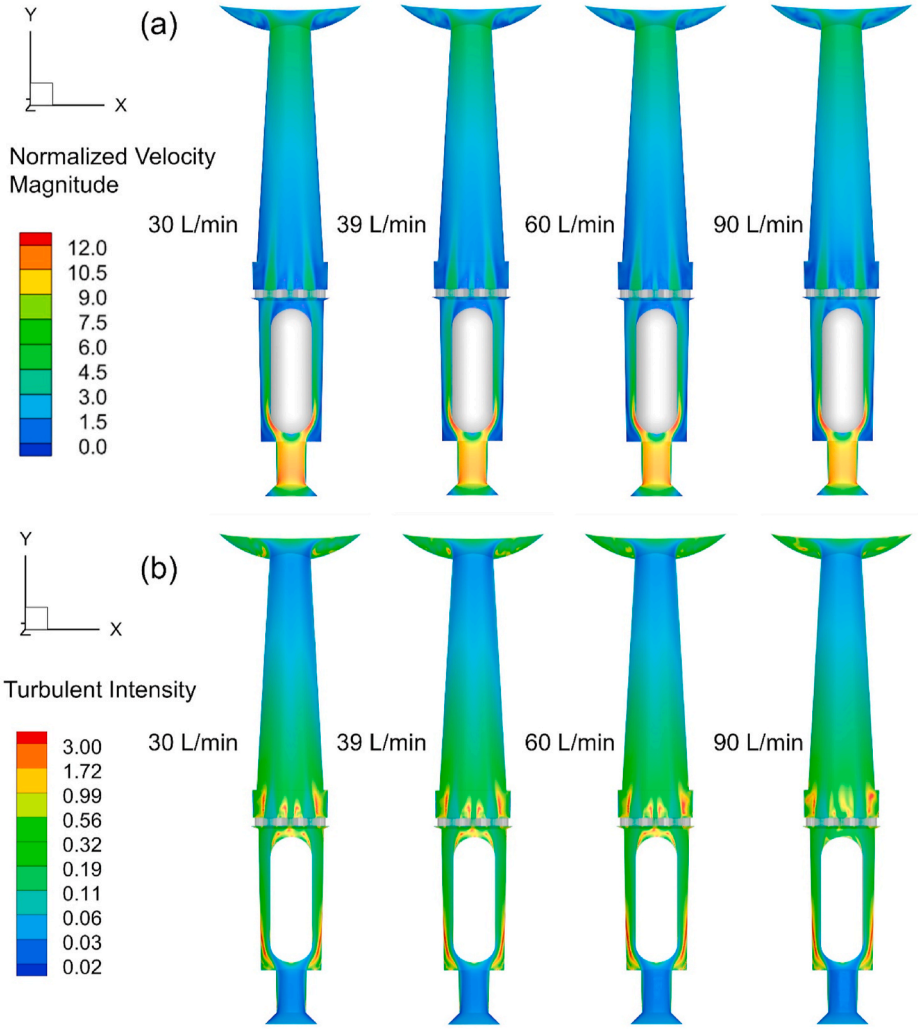


**Fig. 13.** Flow pattern at plane z = 0 in the generic DPI flow channel at different actuation flow rates ($Q_{in}$ = 30, 39, 60, and 90 L/min): (a) normalized velocity magnitude contours ($\overrightarrow{V}/\overrightarrow{V_{out}}$), and (b) turbulent intensity (TI) distributions.

following sections.

### *4.7. Particle deposition in the generic DPI flow channel and DPI delivery efficiency*

Particle deposition distributions in the generic DPI with different $Q_{in}$ and AR = 1 are shown in Fig. 14. Similar to the deposition distributions in SH (see Fig. 6), when 30 L/min ≤ $Q_{in}$≤60 L/min, both API and lactose depositions scattered in the capsule chamber and the extending channel downstream to the grid. When $Q_{in}$ = 90 L/min, the number of particles deposited is significantly reduced, and the majority of particles were emitted from the mouthpiece. However, two main differences in the particle deposition distributions can be found between the CFD-DEM results in the generic and SH DPIs (see Figs. 6 and 14), i.e., (1) For the generic DPI with 30 L/min ≤ $Q_{in}$≤60 L/min, more API and lactose particles deposited in the extending channel downstream to the grid than in the SH DPI, since the cone-shaped extending channel may increase the chance of the particles hitting the wall; and (2) Compared with the SH case with $Q_{in}$ = 60 L/min (see Fig. 6), fewer particle depositions are located at the bottom region of the capsule chamber in the generic DPI (see Fig. 14). The possible reason is that the TI in the bottom region of the capsule chamber of the generic DPI is lower than that of the SH DPI. Hence, less deposition is induced by the turbulent dispersion.

To assess the comparability of the two DPIs on delivery efficiency, comparisons of DFs of both API and lactose in between the flow channels of the generic and SH DPIs are presented in Fig. 15 (a) and (b). Fig. 15 (a) shows that the generic DPI has more API depositions in the device than SH at $Q_{in}$ = 30 L/min, and it has fewer API depositions in the device than SH at $Q_{in}$ = 39, 60, and 90 L/min. It indicates that at a relatively higher actuation flow rate, the generic DPI design has a relatively higher API delivery efficiency than SH. It is worth mentioning that at $Q_{in}$ = 90 L/min, $DF_{API}$ is very close in percentage between the generic and SH DPIs, which indicates that the

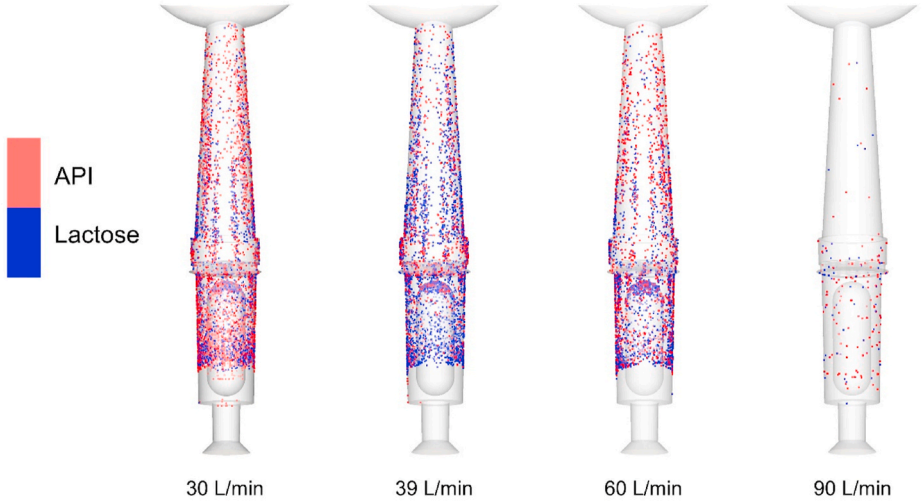


**Fig. 14.** Deposition distributions of API and lactose particles (AR = 1) in the generic DPI at different actuation flow rates ($Q_{in}$ = 30, 39, 60, and 90 L/min).

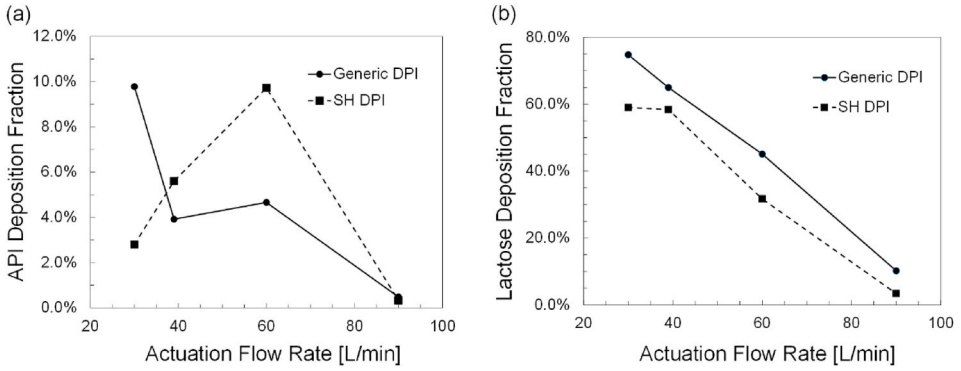


**Fig. 15.** Comparisons of particle deposition fractions (DFs) *vs.* actuation flow rate in the flow channels of the generic DPI and SH DPI: (a) API, and (b) lactose.

flow convection effect is strong enough to overcome the surface energy between API and the device walls with different designs. Furthermore, Fig. 15 (b) compares $DF_{lactose}$ in between the two DPIs for lactose with AR = 1. It can be observed that both DPIs show that the $DF_{lactose}$ decreases with $Q_{in}$. SH predicts relatively lower $DF_{lactose}$ than generic DPI, indicating higher lactose delivery efficiency. This could be due to the different structural designs of the two DPIs. Specifically, more lactose deposit on the wall of the extending channel and the grid region with generic DPI than with SH. Therefore, it can be concluded that the generic DPI's performance at $Q_{in}$ = 90 L/min on both API and lactose delivery efficiencies are close to SH. However, at $Q_{in}$ = 30, 39, and 60 L/min, the performances of the generic and SH DPIs are not very similar.

### *4.8. Assessment of the comparability between the generic and SH DPIs on emitted APSDs*

To further evaluate the similarity between the two DPIs, Fig. 16 shows the emitted APSDs from the generic DPI with different $Q_{in}$. By comparing the APSD predicted by the generic DPI (see Fig. 16) and the SH DPI (see Fig. 9 (a)) for 30 L/min $\leq Q_{in} \leq$ 90 L/min, two observations can be made, i.e., (1) In general, similar APSDs are generated using both DPIs for $Q_{in}$ ranges from 30 L/min to 90 L/min, which indicates that the generic DPI has a high potential to show comparability, (2) The generic DPI, however, predicts slightly higher NFs for small particles (i.e., API), and lower NFs for large particles (i.e., lactose).

### *4.9. Comparability of the generic and SH DPIs for airway depositions*

The similarity between the generic and SH DPIs in airway depositions is evaluated by comparing the lactose and API deposition distribution and their regional DFs in the 3D human respiratory system. Fig. 17 (a) shows the lactose lung deposition distribution using the generic DPI. Like the predicted lung deposition data using SH (see Fig. 11 (a)), all the lactose particles were deposited in the mouth-

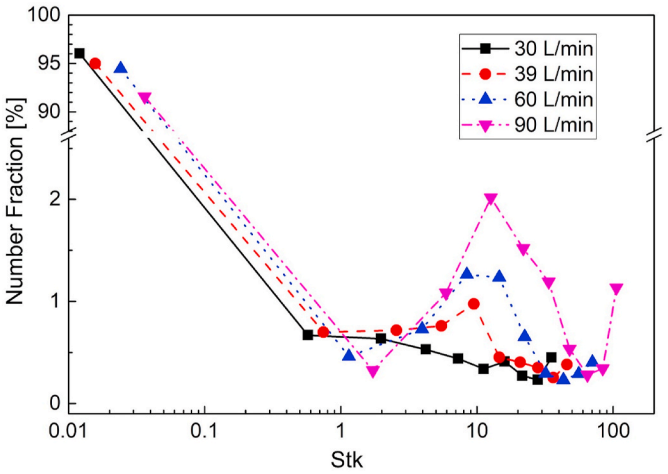


**Fig. 16.** An example of emitted APSDs from the generic DPI with different lactose for spherical lactose carriers (AR = 1) with different actuation flow rates ($Q_{in}$ = 30, 39, 60, and 90 L/min).

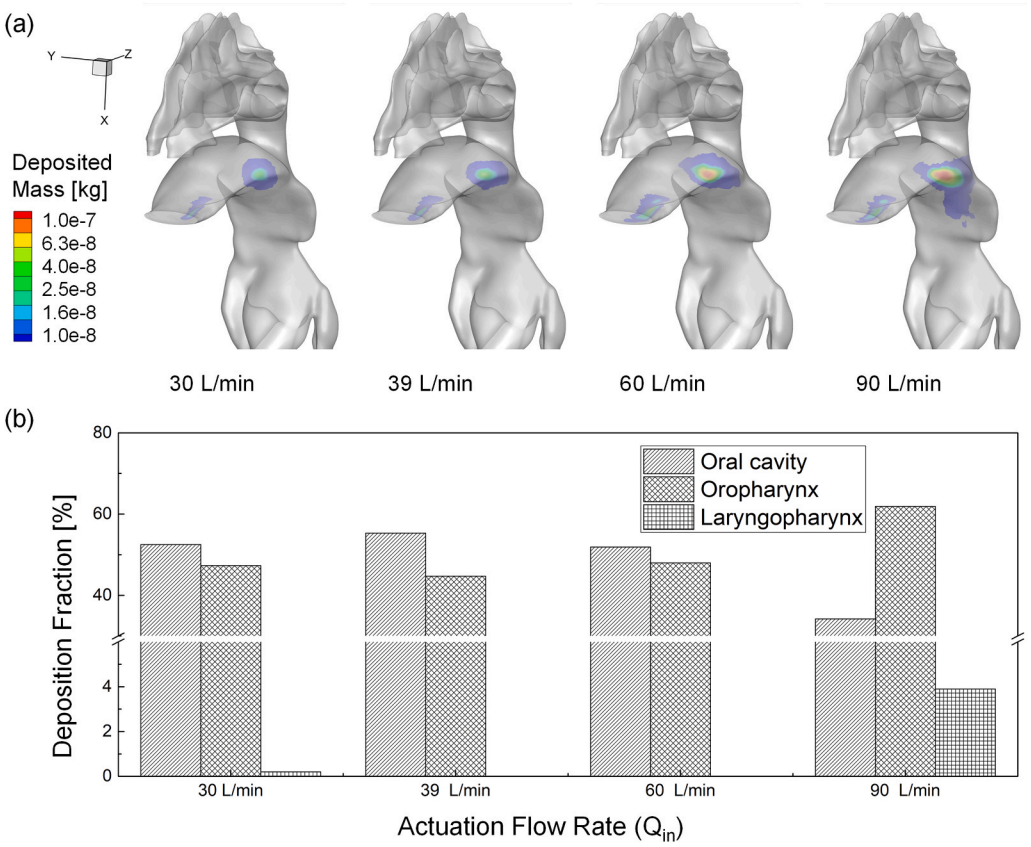


**Fig. 17.** Sample Lactose deposition patterns in the upper airway at different actuation flow rates ($Q_{in}$ = 30, 39, 60, and 90 L/min) using the generic DPI with lactose AR = 1: (a) deposition distributions, and (b) regional deposition fractions (RDFs).

to-throat region, due to the dominant inertial impaction and gravitational sedimentation effects for relatively large lactose particles. Using the generic DPI, the deposition in the oral cavity also concentrates on the tongue due to the gravitational sedimentation of large particles. The unpreferred deposition on the tongue can be reduced by minimizing the angle between the axial direction of the DPI and the centerline of the oral cavity passage. The rest of the lactose particles were carried by the airflow and impacted the oropharynx and deposited. As $Q_{in}$ increases in the generic DPI, the deposition concentration of lactose in the oropharynx also increases due to the more

substantial inertial impaction effect, which is similar to the cases using SH. When comparing the regional DFs of lactose in the human respiratory system upon using the generic and SH DPIs (see Fig. 11 (b) with AR = 1 and Fig. 17 (b)), lung deposition using the generic DPI has a higher$DF_{lactose-oralcavity}$ than $DF_{lactose-oropharynx}$. In comparison, the SH resultant depositions have a lower $DF_{lactose-oral\ cavity}$ than $DF_{lactose-oropharynx}$ at 30 L/min $\leq Q_{in} \leq$60 L/min. The reason for this difference is the difference in emitted APSD generated by the two DPIs. Specifically, the generic DPI generates a higher percentage of large lactose (i.e., $d_p \geq$70 μm) than SH (see Fig. 9 (a) and Fig. 16). Hence, when the $Q_{in}$ is not sufficiently high to generate a dominant convection effect, the gravitational sedimentation effect will lead to more depositions for the particle distributions with more particles larger than 70 μm. At $Q_{in}$ = 90 L/min, the generic DPI case predicts 16.5% lower in $DF_{lactose-oral\ cavity}$ and 20.3% higher in $DF_{lactose-oropharynx}$ than the SH case, even though the generic DPI generates 10.2% more large lactose (i.e., $d_p \geq$70 μm) than SH. This difference could possibly be induced by (1) the dominant convection effect induced higher inertial impaction effect in the oropharynx, and (2) the different designs of the DPI mouthpiece between generic and SH DPIs (see Fig. 1 (a) and (b)), which leads to different particle injection area at the human mouth opening.

The deposition distributions and regional DFs of API in the human respiratory system using the generic DPI are shown in Fig. 18 (a) and (b), which were compared with the API deposition using SH (see Fig. 12 (a) and (b)). The API lung deposition predicted by generic DPI agrees well with the results predicted in the SH cases well (see Fig. 12 with AR = 1). The differences in regional lung $DF_{API}$ for all three airway regions (see Fig. 12 (b) and Fig. 18 (b)) between generic and SH cases are within 2.0% at 30 L/min $\leq Q_{in} \leq$90 L/min. To examine the overall device-airway delivery efficiency, $\psi$ is also calculated for the generic DPI and listed in Table 4. The $\psi$ comparisons between SH and the generic DPI using spherical lactose carriers (AR = 1) demonstrate that $\psi$ generated from the generic DPI has good agreement with the SH at actuation flow rates from 30 to 90 L/min. Specifically, at 39 L/min $\leq Q_{in} \leq$90 L/min, the difference in $\psi$ between generic and SH cases is less than 1.5%. Only at the low actuation flow rate (i.e., 30 L/min), there is a slightly higher difference in $\psi$ between two cases (5.7%) due to the relatively lower delivery efficiency of the generic DPI at $Q_{in}$ = 90 L/min. Therefore, it can be concluded that the generic DPI has satisfactory agreement with the SH DPI in terms of the general DPI-airway drug delivery efficiency.

## 5. Conclusions

In this study, a calibrated and validated numerical approach has been developed based on the CFD-DEM and CFPD models and employed to predict the transport, interaction, and deposition of API and lactose carrier particles with different shapes from the flow channels of two DPIs into a 3D human respiratory system. DPI delivery efficiencies, emitted APSDs, and lung deposition data were obtained and compared between the two DPIs for assessing their comparability. The “all-in-one” modeling framework developed in

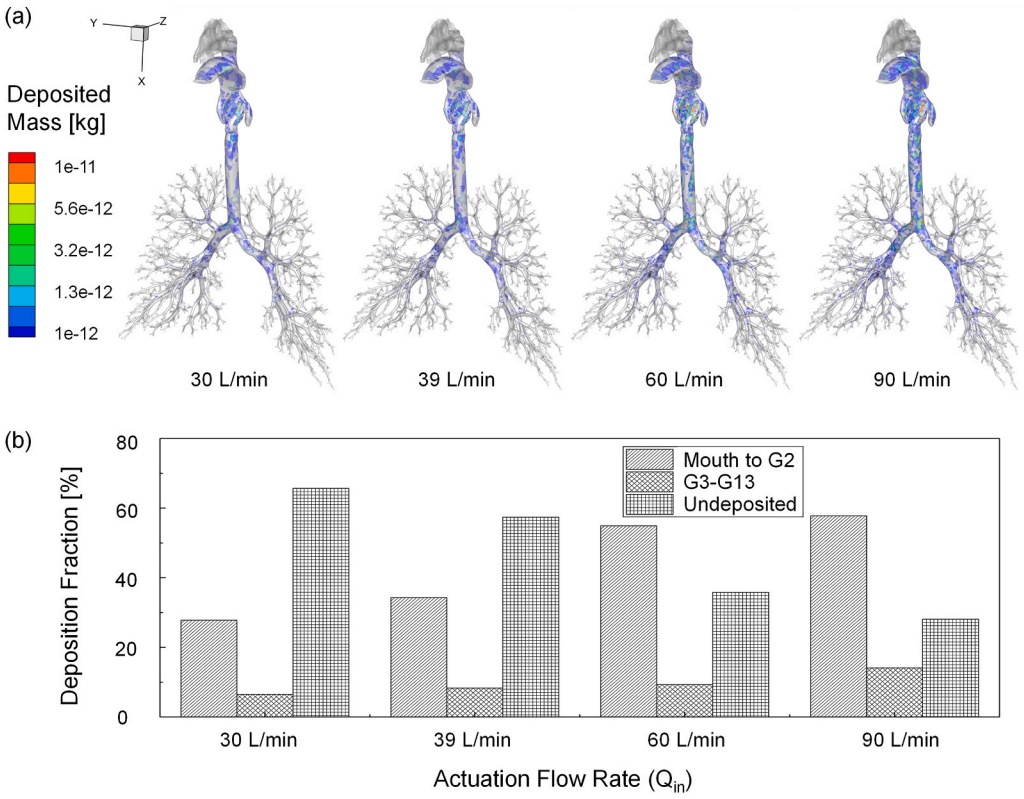


**Fig. 18.** Sample API deposition patterns in the human respiratory system at different actuation flow rates ($Q_{in}$ = 30, 39, 60, and 90 L/min) using the generic DPI and lactose AR = 1: (a) deposition distributions, and (b) regional deposition fractions (RDFs).

this study has the potential to numerically generate *in vitro*-lung deposition correlations, reduce the cost of generic product innovations, and accelerate generic product review and approval. The following inferences can be drawn from the numerical studies and comparisons, i.e.,

(1) With the same particle volume, the shape of lactose carriers can significantly influence the API and lactose deposition in the SH DPI and the DPI delivery efficiency, without a monotonic trend, due to the complex resuspension effect after deposition. The SH DPI delivery efficiency decreases with $Q_{in}$ increasing from 30 to 60 L/min, and then increases up to 95% when the $Q_{in}$ reaches 90 L/min.
(2) The shape effect of lactose carriers is not significant on the API lung deposition patterns. A low actuation flow rate, i.e., $Q_{in} = 30$ L/min, is preferred in enhancing the overall DPI-airway drug delivery efficiency.
(3) Using lactose carriers with AR = 1, comparability between the generic DPI and SH is satisfying at 30 L/min $\leq Q_{in} \leq$90 L/min, based on the good agreements in the overall DPI-airway delivery efficiency, emitted APSDs, as well as the API lung deposition data, with relatively larger differences at $Q_{in} = 30$ L/min with noticeable differences in DPI delivery efficiency, emitted APSDs, and the API lung deposition data.

## 6. Limitations of the study and future work

The CFD-DEM and CFPD models in this study are a first effort for the development of an *in silico* modeling framework to understand OIDP transport dynamics in both the DPI and the human respiratory systems. Though valuable insights have been gained, further work is necessary for its application to a more generalized and physiologically realistic modeling strategy by considering the particle transport dynamics that were not considered in this first effort. Future work may include investigating the particle-laden airflow transport phenomena in DPIs and human respiratory systems using the CFD-DEM modeling framework and a disease-specific lung model. Specifically, the following mechanisms will be considered in the next version of the CFD-DEM modeling effort, i.e.,

(1) Rattling capsule effect on DPI delivery efficiency/particle DF will be modeled using either the semi-resolved CFD-DEM approach or two-way fluid-structure interactions (FSI) in the DPI flow channel.
(2) The mixing process between APIs and lactose carriers can be explicitly simulated in the future using two-way coupled CFD-DEM in the capsule.
(3) The particle size change dynamics due to the condensation/evaporation effects will be captured (Chen, Feng, Zhong, & Kleinstreuer, 2017; Feng et al., 2015; Ferron, Upadhyay, Zimmermann, & Karg, 2013; Haghnegahdar et al., 2019 a) in human respiratory systems.
(4) Instead of constant inhalation flow rate and static lung, patient-specific and disease-specific breathing waveforms for drug inhalation will be employed, and the physiologically realistic airway deformation kinematics will be simulated simultaneously with the particle transport from mouth/nose to alveoli covering the entire pulmonary route (Zhao, Yu, Koshiyama, Wu, 2021).
(5) Excessive secretion and/or stagnation of mucus effects on the airflow structures and particle deposition pattern in airways will be considered (Rajendran & Banerjee, 2019; Yi, Wang, & Feng, 2021) via Volume of Fluid (VOF) plus DPM (Farokhipour, Mansoori, Saffar-Avval, & Ahmadi, 2020).
(6) PK and PD equivalence will be assessed by employing CFPD-PBPK/PD modeling frameworks (Haghnegahdar et al., 2018; Haghnegahdar et al., 2019 a) in the future.

## Declaration of competing interest

The authors declare that they have no known competing financial interests or personal relationships that could have appeared to influence the work reported in this paper.

## Acknowledgment

The research was made possible by funding through the award for project number HR19-106, from the Oklahoma Center for the Advancement of Science and Technology and the award provided by Cipla Inc. (Mumbai, India). The use of Rocky DEM (ESSS, Woburn, MA) as part of the ESSS-CBBL academic partnership is gratefully acknowledged (Dr. Rahul Bharadwaj). The use of Ansys software (Ansys Inc., Canonsburg, PA) as part of the Ansys-CBBL academic partnership is also gratefully acknowledged (Dr. Thierry Marchal). The authors would like to thank Mrs. Pam Reynolds (Engineering Research Proposal Editor and Writer, College of Engineering, Architecture and Technology, Oklahoma State University) for constructive criticism of the manuscript.

## Appendix A. Supplementary data

Supplementary data to this article can be found online at https://doi.org/10.1016/j.jaerosci.2021.105899.

## References


Alzahrany, M., & Banerjee, A. (2015). Aerosolized drug delivery in patient-specific lung model during invasive high frequency oscillatory ventilation. *Journal of Aerosol Science, 81*, 1–20. https://doi.org/10.1016/j.jaerosci.2014.11.005

Bassam, F., York, P., Rowe, R., & Roberts, R. (1990). Young's modulus of powders used as pharmaceutical excipients. *International Journal of Pharmaceutics, 64*(1), 55–60. https://doi.org/10.1016/0378-5173(90)90178-7

Benque, B., & Khinast, J. G. (2021). Estimating inter-patient variability of dispersion in dry powder inhalers using CFD-DEM simulations. *European Journal of Pharmaceutical Sciences, 156*, 105574. https://doi.org/10.1016/j.ejps.2020.105574

Çalış, S., Öztürk Atar, K., Arslan, F. B., Eroğlu, H., & Çapan, Y. (2019). Chapter 4 - nanopharmaceuticals as drug-delivery systems: For, against, and current applications. In Mohapatra, S.S., Ranjan, S., Dasgupta, N., Mishra, R.K., & Thomas, S. (Eds.), Nanocarriers for drug delivery (1st ed., pp. 133–154). *ElsevierNanocarriers for Drug Delivery*. https://doi.org/10.1016/B978-0-12-814033-8.00004-7

Calvert, G., Hassanpour, A., & Ghadiri, M. (2011). Mechanistic analysis and computer simulation of the aerodynamic dispersion of loose aggregates. *Chemical Engineering Research and Design, 89*(5), 519–525. https://doi.org/10.1016/j.cherd.2010.08.013

Carrillo, J.-M. Y., Raphael, E., & Dobrynin, A. V. (2010). Adhesion of nanoparticles. *Langmuir, 26*(15), 12973–12979. https://doi.org/10.1021/la101977c

CDER. (2017). *Draft Guidance on tiotropium bromide*. https://www.accessdata.fda.gov/drugsatfda_docs/psg/Tiotropium%20bromide_inhalation%20powder_NDA%20021395_RC10-17.pdf.

Chen, X., Feng, Y., Zhong, W., & Kleinstreuer, C. (2017). Numerical investigation of the interaction, transport and deposition of multicomponent droplets in a simple mouth-throat model. *Journal of Aerosol Science, 105*, 108–127. https://doi.org/10.1016/j.jaerosci.2016.12.001

Chew, N. Y. K., & Chan, H.-K. (2001). In vitro aerosol performance and dose uniformity between the Foradile® Aerolizer® and the Oxis® turbuhaler. *Journal of Aerosol Medicine, 14*(4), 495–501. https://doi.org/10.1089/08942680152744703

Chow, A. H. L., Tong, H. H. Y., Chattopadhyay, P., & Shekunov, B. Y. (2007). Particle engineering for pulmonary drug delivery. *Pharmaceutical Research, 24*(3), 411–437. https://doi.org/10.1007/s11095-006-9174-3

Delvadia, R. R., Wei, X., Longest, P. W., Venitz, J., & Byron, P. R. (2016). In vitro tests for aerosol deposition. IV: Simulating variations in human breath profiles for realistic DPI testing. *Journal of Aerosol Medicine and Pulmonary Drug Delivery, 29*(2), 196–206. https://doi.org/10.1089/jamp.2015.1215

DFE Pharma. (2006). *Lactose: some basic properties and characteristics*. Retrieved online on. https://www.dfepharma.com/-/media/documents/technical-documents/technical-papers/lactose-some-basic-properties.pdf.

Diulgheroff, N., Scarpitta, F., Pontiroli, A., Kovacsne-Mezei, A., Aronhime, J., & Jegorov, A. (2012). *Forms of tiotropium bromide and processes for preparation thereof: Google Patents*.

Farokhipour, A., Mansoori, Z., Saffar-Avval, M., & Ahmadi, G. (2020). 3D computational modeling of sand erosion in gas-liquid-particle multiphase annular flows in bends. *Wear, 450*, 203241. https://doi.org/10.1016/j.wear.2020.203241

FDA, U. S. (2004). *Spiriva HandiHaler (tiotropium bromide) inhalation powder*. Retrieved from https://www.accessdata.fda.gov/drugsatfda_docs/label/2009/021395s029lbl.pdf.

Feng, Y., & Kleinstreuer, C. (2013). Analysis of non-spherical particle transport in complex internal shear flows. *Physics of Fluids, 25*(9), Article 091904. https://doi.org/10.1063/1.4821812

Feng, Y., & Kleinstreuer, C. (2014). Micron-particle transport, interactions and deposition in triple lung-airway bifurcations using a novel modeling approach. *Journal of Aerosol Science, 71*, 1–15. https://doi.org/10.1016/j.jaerosci.2014.01.003

Feng, Y., Kleinstreuer, C., Castro, N., & Rostami, A. (2016). Computational transport, phase change and deposition analysis of inhaled multicomponent droplet–vapor mixtures in an idealized human upper lung model. *Journal of Aerosol Science, 96*(6), 96–123. https://doi.org/10.1016/j.jaerosci.2016.03.001

Feng, Y., Kleinstreuer, C., & Rostami, A. (2015). Evaporation and condensation of multicomponent electronic cigarette droplets and conventional cigarette smoke particles in an idealized G3–G6 triple bifurcating unit. *Journal of Aerosol Science, 80*, 58–74. https://doi.org/10.1016/j.jaerosci.2014.11.002

Feng, Y., Marchal, T., Sperry, T., & Yi, H. (2020). Influence of wind and relative humidity on the social distancing effectiveness to prevent COVID-19 airborne transmission: A numerical study. *Journal of Aerosol Science*, 105585. https://doi.org/10.1016/j.jaerosci.2020.105585

Feng, Y., Zhao, J., Hayati, H., Sperry, T., & Yi, H. (2021). Tutorial: Understanding the transport, deposition, and translocation of particles in human respiratory systems using Computational Fluid-Particle Dynamics and Physiologically Based Toxicokinetic models. *Journal of Aerosol Science, 151*, 105672. https://doi.org/10.1016/j.jaerosci.2020.105672

Feng, Y., Zhao, J., Kleinstreuer, C., Wang, Q., Wang, J., Wu, D. H., et al. (2018). An in silico inter-subject variability study of extra-thoracic morphology effects on inhaled particle transport and deposition. *Journal of Aerosol Science, 123*, 185–207. https://doi.org/10.1016/j.jaerosci.2018.05.010

Ferron, G. A., Upadhyay, S., Zimmermann, R., & Karg, E. (2013). Model of the deposition of aerosol particles in the respiratory tract of the rat. II. Hygroscopic particle deposition. *Journal of Aerosol Medicine and Pulmonary Drug Delivery, 26*(2), 101–119. https://doi.org/10.1089/jamp.2011.0965

Haghnegahdar, A., Feng, Y., Chen, X., & Lin, J. (2018). Computational analysis of deposition and translocation of inhaled nicotine and acrolein in the human body with e-cigarette puffing topographies. *Aerosol Science and Technology, 52*(5), 483–493. https://doi.org/10.1080/02786826.2018.1447644

Haghnegahdar, A., Zhao, J., & Feng, Y. (2019a). Lung aerosol dynamics of airborne influenza A virus-laden droplets and the resultant immune system responses: An in silico study. *Journal of Aerosol Science, 134*, 21.

Haghnegahdar, A., Zhao, J., Kozak, M., Williamson, P., & Feng, Y. (2019b). Development of a hybrid CFD-PBPK model to predict the transport of xenon gas around a human respiratory system to systemic regions. *Heliyon, 5*(4), e01461. https://doi.org/10.1016/j.heliyon.2019.e01461. e01461.

Hayati, H., Feng, Y., & Hinsdale, M. (2021). Inter-species variabilities of droplet transport, size change, and deposition in human and rat respiratory systems: An in silico study. *Journal of Aerosol Science, 154*, 105761. https://doi.org/10.1016/j.jaerosci.2021.105761

Horabik, J., & Molenda, M. (2016). Parameters and contact models for DEM simulations of agricultural granular materials: A review. *Biosystems Engineering, 147*, 206–225. https://doi.org/10.1016/j.biosystemseng.2016.02.017

Johnson, R. W. (2016). *Handbook of fluid dynamics*. Crc Press.

Jiang, M., Dai, Y., Cui, L., & Xi, B. (2018). Experimental and DEM analyses on wheel-soil interaction. *Journal of Terramechanics, 76*, 15–28. https://doi.org/10.1016/j.jterra.2017.12.001

Johnson, K. L., Kendall, K., Roberts, A. D., & Tabor, D. (1971). Surface energy and the contact of elastic solids. *Proceedings of the Royal Society of London. A. Mathematical and Physical Sciences, 324*(1558), 301–313. https://doi.org/10.1098/rspa.1971.0141

Kinnunen, H., Hebbink, G., Peters, H., Shur, J., & Price, R. (2014). An investigation into the effect of fine lactose particles on the fluidization behaviour and aerosolization performance of carrier-based dry powder inhaler formulations. *AAPS PharmSciTech, 15*(4), 898–909. https://doi.org/10.1208/s12249-014-0119-6

Kleinstreuer, C., Zhang, Z., & Donohue, J. (2008). Targeted drug-aerosol delivery in the human respiratory system. *Annual Review of Biomedical Engineering, 10*, 195–220. https://doi.org/10.1146/annurev.bioeng.10.061807.160544

Koullapis, P., Kassinos, S. C., Muela, J., Perez-Segarra, C., Rigola, J., Lehmkuhl, O., … Nicolaou, L. (2018). Regional aerosol deposition in the human airways: The SimInhale benchmark case and a critical assessment of in silico methods. *European Journal of Pharmaceutical Sciences, 113*, 77–94. https://doi.org/10.1016/j.ejps.2017.09.003

Lee, S. L., Saluja, B., García-Arieta, A., Santos, G. M. L., Li, Y., Lu, S., … Lyapustina, S. (2015). Regulatory considerations for approval of generic inhalation drug products in the US, EU, Brazil, China, and India. *The AAPS Journal, 17*(5), 1285–1304. https://doi.org/10.1208/s12248-015-9787-8

Lewis, D., Rouse, T., Singh, D., & Edge, S. (2017). Defining the 'dose' for dry powder inhalers: The challenge of correlating in-vitro dose delivery results with clinical efficacy. *American Pharmaceutical Review, 20*, 54–62.

Li, A., & Ahmadi, G. (1993). Deposition of aerosols on surfaces in a turbulent channel flow. *International Journal of Engineering Science, 31*(3), 435–451. https://doi.org/10.1016/0020-7225(93)90017-O

Longest, P. W., Bass, K., Dutta, R., Rani, V., Thomas, M. L., El-Achwah, A., et al. (2019). Use of computational fluid dynamics deposition modeling in respiratory drug delivery. *Expert Opinion on Drug Delivery, 16*(1), 7–26. https://doi.org/10.1080/17425247.2019.1551875

Meng, H.-q., Chen, L., & Chen, D.-h. (2019). Effect of carrier size and surface morphology on the aerosolization of formulation in a capsule-based dry powder inhaler. *Acta Pharmaceutica Sinica, 54*(9), 1673–1679.

Menter, F., & Lechner, R. (2019). *Best Practice: Generalized k-omega two-Equation turbulence model in Ansys CFD (GEKO)*. Ansys. https://fluidcodes.com/wp-content/uploads/2020/06/geko-tp-1.pdf.

Mindlin, R. D., & Deresiewicz, H. (1953). Elastic spheres in contact under varying oblique forces. *Journal of Applied Mechanics, 20*(3), 327–344. https://doi.org/10.1115/1.4010702

Mitani, R., Ohsaki, S., Nakamura, H., & Watano, S. (2020). Numerical study on particle adhesion in dry powder inhaler device. *Chemical and Pharmaceutical Bulletin, 68*(8), 726–736. https://doi.org/10.1248/cpb.c20-00106

Modenese, C., Utili, S., & Houlsby, G. T. (2012). A study of the influence of surface energy on the mechanical properties of lunar soil using DEM *Discrete Element Modelling of Particulate Media. Royal Society of Chemistry*. https://doi.org/10.1039/9781849735032-00069

Moreno-Atanasio, R. (2012). Energy dissipation in agglomerates during normal impact. *Powder Technology, 223*, 12–18. https://doi.org/10.1016/j.powtec.2011.05.016

Morrissey, J. P. (2013). *Discrete element modelling of iron ore pellets to include the effects of moisture and fines (Doctoral dissertation)*. UK: University of Edinburgh.

Ponzini, R., Da Vià, R., Bnà, S., Cottini, C., & Benassi, A. (2021). Coupled CFD-DEM model for dry powder inhalers simulation: Validation and sensitivity analysis for the main model parameters. *Powder Technology, 385*, 199–226. https://doi.org/10.1016/j.powtec.2021.02.044

Pramanik, S., Mohanto, S., Manne, R., Rajendran, R. R., Deepak, A., Edapully, S. J., & Katari, O. (2021). Nanoparticle-based drug delivery system: The magic bullet for the treatment of chronic pulmonary diseases. *Molecular Pharmaceutics, 18*(10), 3671–3718. https://doi.org/10.1021/acs.molpharmaceut.1c00491

Rajendran, R. R., & Banerjee, A. (2019). Mucus transport and distribution by steady expiration in an idealized airway geometry. *Medical Engineering & Physics, 66*, 26–39. https://doi.org/10.1016/j.medengphy.2019.02.006

Saffman, P. (1965). The lift on a small sphere in a slow shear flow. *Journal of Fluid Mechanics, 22*(2), 385–400. https://doi.org/10.1017/S0022112065000824

Sandell, D. (2021). Bioequivalence assessment of pharmaceutical aerosol products through IVIVC. *Advanced Drug Delivery Reviews*. https://doi.org/10.1016/j.addr.2021.113895

Shimazaki, Y., Okubo, M., Yamamoto, T., & Yoshida, A. (2009). Three-dimensional numerical simulation of nanoparticle inhalation and indoor pollution around breathing human. *Journal of Environment and Engineering, 4*(1), 145–161. https://doi.org/10.1299/jee.4.145

Son, Y.-J., Longest, P. W., Tian, G., & Hindle, M. (2013). Evaluation and modification of commercial dry powder inhalers for the aerosolization of a submicrometer excipient enhanced growth (EEG) formulation. *European Journal of Pharmaceutical Sciences, 49*(3), 390–399. https://doi.org/10.1016/j.ejps.2013.04.011

Tian, G., Hindle, M., Lee, S., & Longest, P. W. (2015). Validating CFD predictions of pharmaceutical aerosol deposition with in vivo data. *Pharmaceutical Research, 32*(10), 3170–3187. https://doi.org/10.1007/s11095-015-1695-1

Tong, Y., & Yu. (2017). CFD-DEM study of the aerosolisation mechanism of carrier-based formulations with high drug loadings. *Powder Technology, 314*, 620–626. https://doi.org/10.1016/j.powtec.2016.10.004

Tong, Z., Yu, C., & Yang. (2016). CFD–DEM investigation of the effect of agglomerate–agglomerate collision on dry powder aerosolisation. *Journal of Aerosol Science, 92*, 109–121. https://doi.org/10.1016/j.jaerosci.2015.11.005

Walenga, R. L., Babiskin, A. H., & Zhao, L. (2019). Silico methods for development of generic drug-device combination orally inhaled drug products. *CPT: Pharmacometrics & Systems Pharmacology, 8*(6), 359–370. https://doi.org/10.1002/psp4.12413

Walton, O. R. (2008). Review of adhesion fundamentals for micron-scale particles. *KONA Powder and Particle Journal, 26*, 129–141. https://doi.org/10.14356/kona.2008012

Wang, Y., Chu, K., & Yu, A. (2017). Transport and deposition of cohesive pharmaceutical powders in human airway. In *Paper presented at the EPJ Web of Conferences*.

Yang, J., Wu, C.-Y., & Adams, M. (2015). Numerical modelling of agglomeration and deagglomeration in dry powder inhalers: A review. *Current Pharmaceutical Design, 21*(40), 5915–5922. https://doi.org/10.2174/1381612821666151008150845

Yi, H., Wang, Q., & Feng, Y. (2021). Computational analysis of obstructive disease and cough intensity effects on the mucus transport and clearance in an idealized upper airway model using the volume of fluid method. *Physics of Fluids, 33*(2), Article 021903. https://doi.org/10.1063/5.0037764

Zellnitz, S., Zellnitz, L., Müller, M. T., Meindl, C., Schröttner, H., & Fröhlich, E. (2019). Impact of drug particle shape on permeability and cellular uptake in the lung. *European Journal of Pharmaceutical Sciences, 139*, 105065. https://doi.org/10.1016/j.ejps.2019.105065

Zhang, Z., & Kleinstreuer, C. (2011). Laminar-to-turbulent fluid–nanoparticle dynamics simulations: Model comparisons and nanoparticle-deposition applications. *International Journal for Numerical Methods in Biomedical Engineering, 27*(12), 1930–1950. https://doi.org/10.1002/cnm.1447

Zhang, Z., Kleinstreuer, C., & Feng, Y. (2012). Vapor deposition during cigarette smoke inhalation in a subject-specific human airway model. *Journal of Aerosol Science, 53*, 40–60. https://doi.org/10.1016/j.jaerosci.2012.05.008

Zhao, J., Feng, Y., Bezerra, M., Wang, J., & Sperry, T. (2019). Numerical simulation of welding fume lung dosimetry. *Journal of Aerosol Science*. https://doi.org/10.1016/j.jaerosci.2019.05.006

Zhao, J., Feng, Y., & Fromen, C. A. (2020). Glottis motion effects on the particle transport and deposition in a subject-specific mouth-to-trachea model: A CFPD study. *Computers in Biology and Medicine, 116*, 103532.

Zhao, J., Feng, Y., Tian, G., Taylor, C., & Arden, N. S. (2021). Influences of puff protocols and upper airway anatomy on cannabis pharmacokinetics: A CFPD-PK study. *Computers in Biology and Medicine, 132*, 104333. https://doi.org/10.1016/j.compbiomed.2021.104333

Zhao, J., Feng, Y., Koshiyama, K., & Wu, H. (2021). Prediction of Airway Deformation Effect on Pulmonary Air-Particle Dynamics: A Numerical Study. *Physics of Fluids, 33*, 101906. https://doi.org/10.1063/5.0065309

Zheng, Z., Leung, S. S. Y., & Gupta, R. (2021). Flow and particle modelling of dry powder inhalers: Methodologies, recent development and emerging applications. *Pharmaceutics, 13*(2), 189. https://doi.org/10.3390/pharmaceutics13020189

Zuurman, K., Riepma, K., Bolhuis, G., Vromans, H., & Lerk, C. (1994). The relationship between bulk density and compactibility of lactose granulations. *International Journal of Pharmaceutics, 102*(1–3), 1–9. https://doi.org/10.1016/0378-5173(94)90033-7